DOE/JPL 954739-4

Annual Report SC5106.104AR

Period Covered: January 1, 1980 through December 31, 1980

STUDY PROGRAM FOR ENCAPSULATION MATERIALS INTERFACE FOR LOW-COST SOLAR ARRAY

To

Jet Propulsion Laboratory
California Institute of Technology

for the

Encapsulation Task of the Low-Cost
Solar Array Project

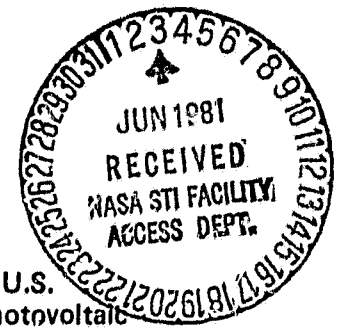

The JPL Low-Cost Solar Array Project is sponsored by the U.S. Department of Energy and forms part of the Solar Photovoltaic Conversion Program to initiate a major effort toward the development of low-cost solar arrays. This work was performed for the Jet Propulsion Laboratory, California Institute of Technology by agreement between NASA and DOE.

This report contains information proposed by the Science Center, Rockwell International, under JPL Subcontract 954739.

February, 1981

D. H. Kaelble, F. B. Mansfeld, M. Kendig, C. Leung

Science Center
Rockwell International
1049 Camino Dos Rios
Thousand Oaks, California 91360

TABLE OF CONTENTS

		Page
	ACKNOWLEDGEMENTS	1
	ABSTRACT	2
1.0	OBJECTIVES	3
2.0	SUMMARY	4
	2.1 Atmospheric Corrosion Model Verification	4
	2.2 AC Impedance Monitoring and Analysis	5
	2.3 Hydrothermal Stress Analysis of Solar Arrays	5
	2.4 Criteria for Encapsulant Bonding	6
3.0	INTRODUCTION	7
4.0	ANALYTICAL MODELS	10
	4.1 Solar Array Current-Voltage (I-V) Model	10
	4.2 AC Impedance Model	16
5.0	EXPERIMENTAL	24
	5.1 Mead Site Atmospheric Corrosion Monitoring	24
	5.2 Hydrothermal Stress Analysis	33
	5.3 Hydrothermal Cell Cracking and Corrosion	46
	5.4 Interfacial Bonding for Corrosion Protection	52
6.0	CONCLUSIONS	55
7.0	RECOMMENDATIONS	57
8.0	NEW TECHNOLOGY	58
9.0	REFERENCES	59
APPENDIX I:	Mathematical Relations for Current-Voltage (I-V) Response in Single Solar Cells	61
APPENDIX II:	Electrical Impedance of Solar Cells and Low Cost Solar Arrays	69

ACKNOWLEDGEMENTS

The authors wish to express their appreciation to the many individuals who contributed to this research and this report. At the Jet Propulsion Laboratory the helpful discussions and supply of test materials by M. Sarboloukí, H. Maxwell, J. Repar and A. Gupta were most helpful. Professor Charles Rogers of Case Western University and Professor Wolfgang Knauss of California Institute of Technology provided progress reports and direct advice to this program. The technical cooperation provided by Steve Forman and his colleagues at the Lincoln Laboratories, M.I.T. were important to the successful completion of the Mead, Nebraska corrosion monitoring experiment.

Jovan Moacanin is technical monitor of this subcontract for JPL and Cliff Coulbert of JPL is Manager of the Encapsulation Task of the Low Cost Solar Array Project. Their helpful technical guidance is greatfully acknowledged.

ABSTRACT

The early validation of a 20 year service integrity for the bonded interface in solar cell modules is an important requirement in the Low Cost Solar Array (LSA) project.

The first annual report (Science Center Report No. SC5106.22AR) outlines and implements a physical/chemical evaluation program for solar cell encapsulants. The results of computer controlled ultrasonic and optical/ellipsometric mapping for interfacial defect characterization in solar modules is summarized in the second annual report (SC5106.49AR). The development and validation of an atmospheric corrosion model and test plan for LSA outdoor service at the Mead, Nebraska test site is presented in the third annual report (SC5106.86AR).

In the present fourth phase of study detailed in this annual report emphasis is placed on the development of AC impedance as a nondestructive evaluation (NDE) methodology for solar arrays and the further development of corrosion models and materials selection criteria for corrosion resistant interfaces.

1.0 OBJECTIVES

The general objective of this phase of the program is to broaden the present corrosion model and atmospheric corrosion studies developed for the Mead, Nebraska test site. The two major objectives included in this present study are stated as follows:

1) Continue further development of atmospheric corrosion monitors and AC impedance measurements as nondestructive evaluation (NDE) tools for LSA module performance and life prediction.

2) Initiate development of materials selection criteria and tests for corrosion protection and environment resistant interfaces as required for validation of corrosion models.

2.0 SUMMARY

2.1 Atmospheric Corrosion Model Verification

a. A 13 month experimental study of climatology and atmospheric corrosion monitoring (ACM) of the Mead, Nebraska LSA test site has been completed.

b. During this 13 month period the ACM units recorded the corrosion protection function of an encapsulant system (a reactive primer GE-SS4155 on Zn/Cu plates encapulated by Sylgard 184).

c. A non-encapsulated ACM unit correlated Mead climatology with corrosion rates as defined by an atmospheric corrosion model.

d. Both the intermediate and final results of this study verify the prediction that atmospheric corrosion rate is the product of the moisture condensation probability (P_c) and the maximum ionic diffusion current (I_L) at the corrosion surface or interface.

e. Encapsulant corrosion protection is specifically related to the suppression of I_L at the potential corrosion interface.

2.2 AC Impedance Monitoring and Analysis

a. A predictive model for solar array current-voltage (I-V) response has been developed and correlated to AC impedance.

b. A new and simplified methodology for conducting AC impedance measurement and spectrum analysis has been developed and verified for nondestructive evaluation of LSA performance.

c. A preliminary design for an AC impedance measurement, spectrum analysis, and performance optimizing control for a solar array branch circuit has been outlined.

2.3 Hydrothermal Stress Analysis of Solar Arrays

a. A computer model for hydrothermal stress analysis (HTSA) has been successfully applied to evaluate the combined effects of temperature-humidity cycling on solar cell cracking mechanism in LSA modules using a fiber board substrate.

b. The protective effect of moisture diffusion barrier coatings of ethylene vinylacetate (EVA) and polytrifluorochloroethylene (KEL-F) is predicted to delay but not change the solar cell cracking process.

2.4 Criteria for Encapsulant Bonding

a. A new criterion for encapsulant bonding is being developed and specifically directed at supressing the microcorrosion process in the presence of internal defects such as micro-cracks.

3.0 INTRODUCTION

In view of the promising early results of the atmospheric corrosion model developed for the low cost solar array (LSA) at the Mead, Nebraska test site the present program was expanded relative to a general LSA life prediction program as shown in Fig. 1. The logic flow diagram of Fig. 1 describes the materials imputs to an LSA system in the upper block. The next lower block describes the environmental stresses known to cause LSA performance degradation. The specific mechanisms of degradation and consequent degradation effects are detailed in the subsequent decending blocks of Fig. 1 with debonding and corrosion near the bottom of the figure and directly connected with photovoltaic reliability and durability. On the right of Fig. 1 are categorized the specialized measurementand analysis programs which correlate with each degradation mechanism and effect.

The prior annual report (SC5106.86AR) details the results of the corrosion program whose scope is defined by the inner bracket on the right of Fig. 1. In this prior program consistant interrelations have identified the corrosion chemistry, changes in the AC impedance spectrum, and the photovoltaic current-voltage (IV) profile which measures photovolaic performance. In the present program the corrosion studies were expanded to include development of a life prediction model and life prediction test plan which included the debonding and corrosion process. This report details the progress of this effort under a Task I which now encompasses corrosion modeling, life prediction in terms of photovoltaic performance and nondestructive evaluation of

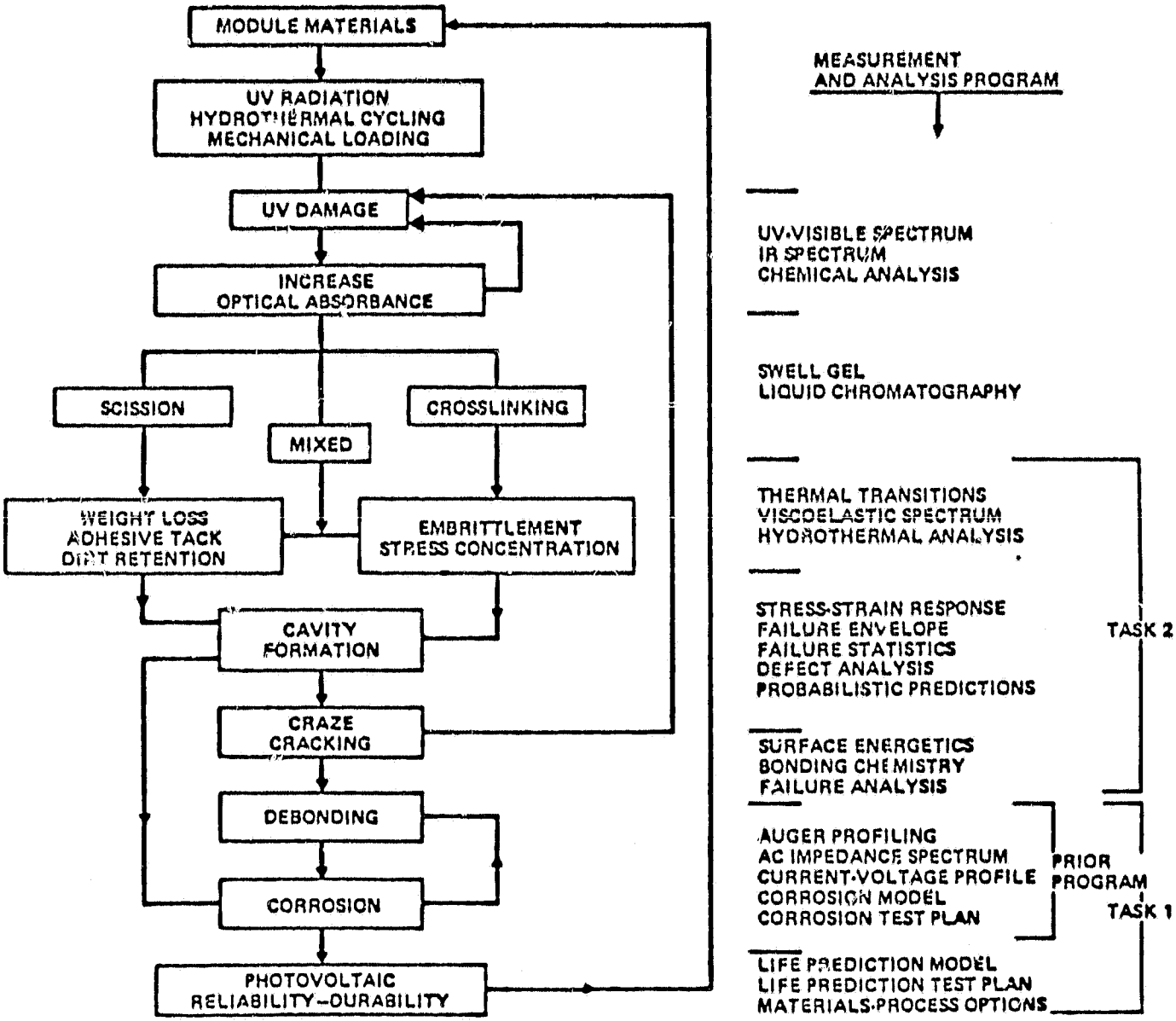

Fig. 1 General LSA life prediction program.

performance of modules and solar array branch circuits. This phase of the study is closely coupled to extensive studies in photovoltaic design optimization already completed by JPL.

In order to provide for new materials selections in terms of advancing LSA technology a new study program in material selection criteria for corrosion resistant bonding in the presences of microdefects has been initiated. This study is defined as Task 2 in the right bracket of Fig. 1. This task implements an already developed computer model[7] for hydrothermal stress analysis (HTSA) to define potential mechanisms of LSA microfailure and to focus the materials studies and bonding criteria to the specific failure mechanisms. In addition, a new physical/chemical bonding criteria and test protocol has been initiated for minimizing ionic conduction at encapsulant interfaces in LSA.

4.0 ANALYTICAL MODELS

Two analytical models have been developed within this program to translate the results of corrosion analysis into predictions of photovoltaic performance and durability. The first of these models develops the current-voltage relations for a singin solar cell performance. By introduction of summing relations for series and parallel interconnection the performance and AC impedance response of a branch circuit can be calculated. The second model is developed for a simplified computational methodology to analyse AC impedance spectrum. The combination of these models provides a potential new basis for nondestructive evaluation (NDE) and feedback control of solar arrays.

4.1 Solar Array Current Voltage (I-V) Model

Appendix I provides a detailed derivation of an analog model for solar cell response which permits direct calculation of the I-V fill factor, maximum power point and other performance properties relating to solar cell response. The equation, diagram and nomenclature of Fig. 2 give a brief synopsis of this I-V response model. Based upon controlled variations of isolation S and temperature T the curves of Fig. 3 show how the design parameters of this I-V response model can be evaluated experimentally. The I-V curves in the upper right portion of Fig. 3 are taken from a published report and represent typical silicon module response.[4] The calibration experiments of Fig. 3 define all of the solar cell design parameters with the exception of R_{SH} and R_S. As documented in the third annual report (SC5106.86AR) AC-impedance

$$I_o = I_d + K_1 S$$

$$V_o = V_d - K_2 (T + K_3 S)$$

$$K = \frac{1}{V_o} \ln\left(\frac{R_s + R_{sh}}{R_s}\right)$$

$$\lambda = 1 - \exp(-KV_o)$$

$$I = \frac{I_o}{\lambda}\left[1 - \exp K(V - V_o)\right]$$

$$R = \frac{-dV}{dI} = \frac{1 - \exp(-KV_o)}{KI_o \exp K(V - V_o)}$$

$$F = \frac{1}{\lambda} - \frac{1}{KV_o}$$

$$\ln(KV_m + 1) + KV_m - KV_o = 0$$

$$W_m = I_o \lambda^{-1} V_m [1 - \exp K(V_m - V_o)]$$

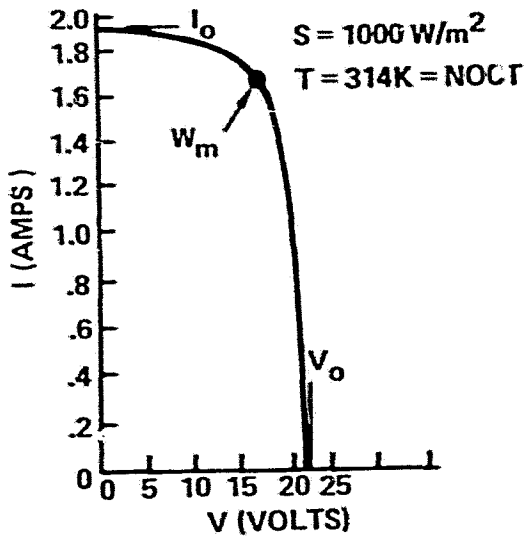

DESIGN PARAMETERS

K_1	COEFFICIENT OF LIGHT DEVELOPED CURRENT
K_2	THERMAL COEFFICIENT OF VOLTAGE
K_3	THERMAL COEFFICIENT OF LIGHT
I_D	DARK CURRENT
V_D	DARK VOLTAGE
R_S	SERIES RESISTANCE
R_{SH}	SHUNT RESISTANCE

ENVIRONMENT PARAMETERS

T	AMBIENT TEMPERATURE
S	AMBIENT INSOLATION

PERFORMANCE VARIABLES

I_o	SHORT CIRCUIT CURRENT
V_o	OPEN CIRCUIT VOLTAGE
K, λ	CURRENT–VOLTAGE (I–V) RESPONSE FACTORS
F	I–V FILL FACTOR
V_m	VOLTAGE AT THE MAXIMUM POWER POINT
W_m	WATTAGE AT THE MAXIMUM POWER POINT
I_m	CURRENT AT THE MAXIMUM POWER POINT
P_m	PROPORTION OF IDEAL POWER OUTPUT

Fig. 2 Current - voltage (I-V) relations solar cell response

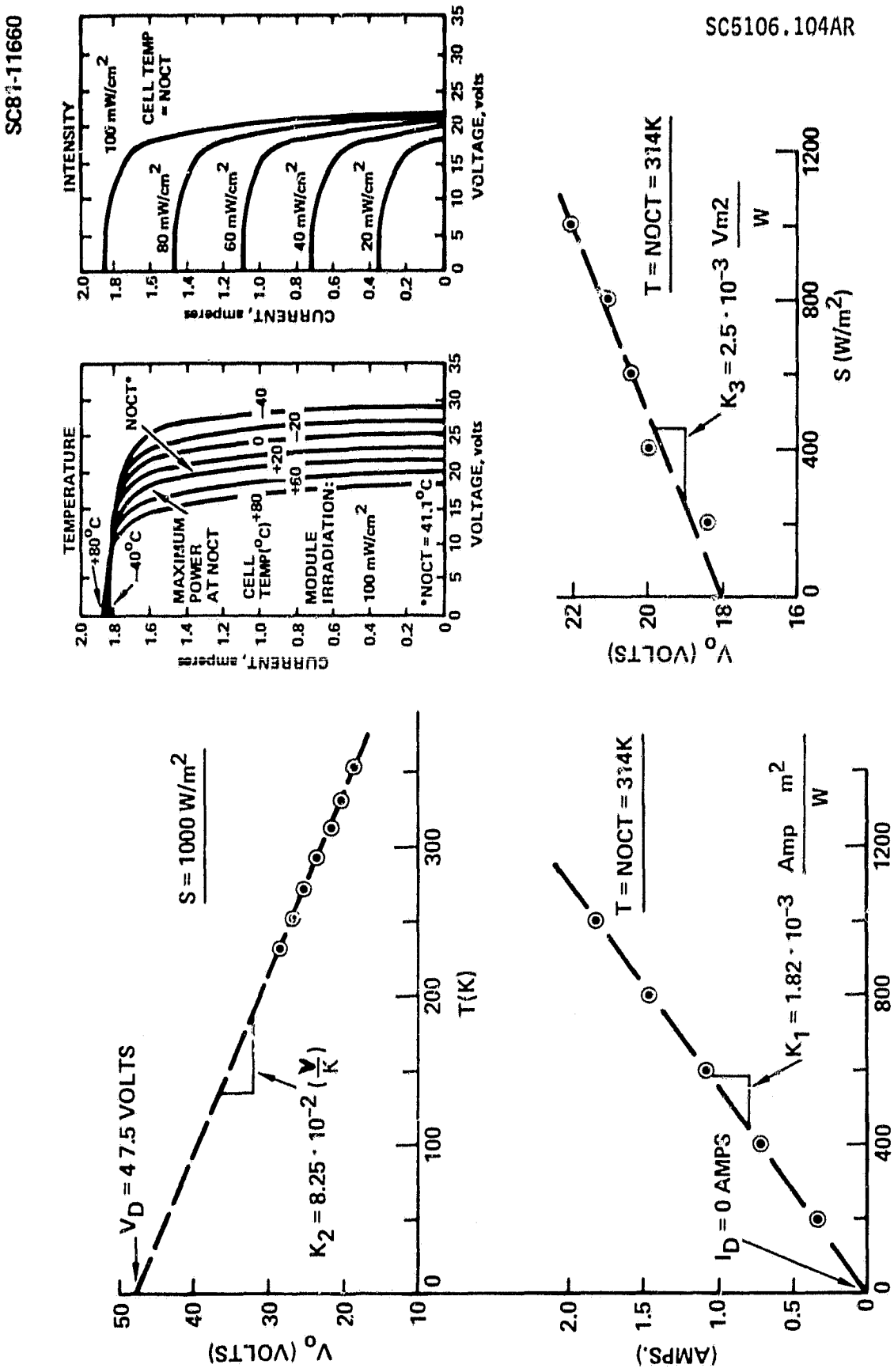

Fig. 3 Evaluation of insolation and thermal coefficients (K_1, K_2, K_3, I_D, V_D).

is very sensitive to small decreases in shunt resistance R_{SH} due to cell corrosion which are not evident in the shape of the I-V performance curve as defined by the fill factor F. The calculated I-V response curves of Fig. 4 illustrate why this experimental result is observed. The right view of Fig. 4 plots the logarithm of R_{SH}/R_S versus the calculated fill factor F. For high performance cells with F>0.8 the right curve of Fig. 4 shows that F is quite insensitive to small changes in $R_{SH}/R_S>100$. The upper left I-V curve of Fig. 4 for $KV_O=10.0$ represents a high performance cell response with F=0.9. The slope of the upper curve at $V/V_O=0$, which is a measure of $-1/(R_{SH}+R_S)$, is so slight as to make shunt resistance measurements impractical from I-V curves.

The mathematical selections and schematic curves of Fig. 5 introduce an AC impedance model for a single solar cell. Extensive experiments now show that single solar cells display a single relaxation time τ and when the storage Z' and loss Z" components of the complex impedance are plotted as in the lower right curve of Fig. 4 a semicircle with a center at Z"=0, Z'= $R_S + R_{SH}/2$ and radius $R_{SH}/2$ results which is termed the Cole-Cole plot.[8] Evaluation of AC impedance data via the Cole-Cole plot isolates the shunt and series resistance for the single solar cell or a solar cell module as prior reports in this program have documented.

In general, as analytical modeling and direct testing have indicated, the presence of mismatches in single cell I-V response within a solar array leads to lowered power efficiency in a solar array.[6-9] The mathematical relations of Fig. 6 illustrate a method for describing statistical variabilities of all solar cell design properties in terms of Weibull

SC81-11661

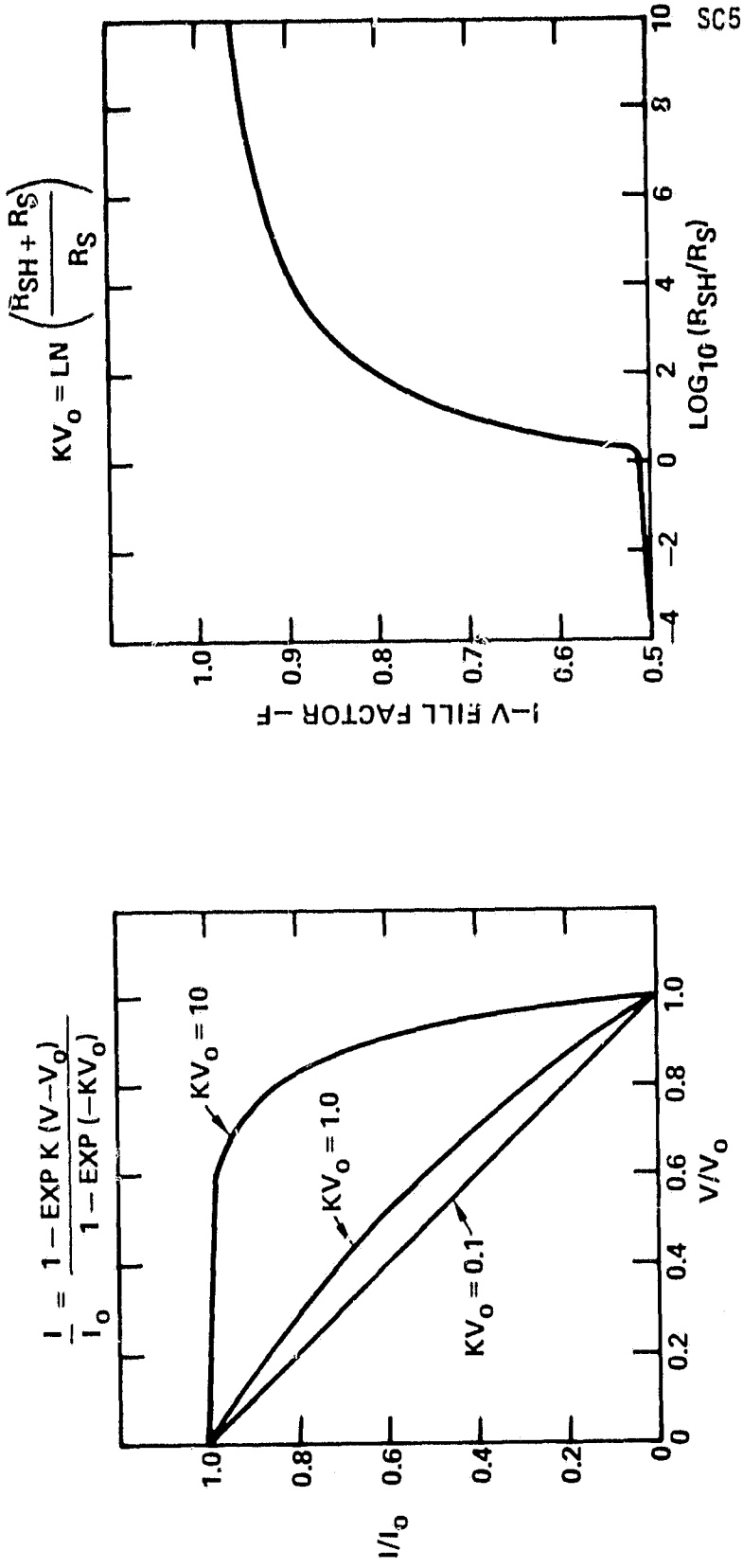

Fig. 4 Calculated current - voltage (I-V) response.

$$Z^* = Z^1 + iZ^{11}$$

$$|Z^*| = \left[(Z^1)^2 + (Z^{11})^2 \right]^{1/2}$$

$$\tau = CR_{SH}$$

$$Z^1 = R_S + \frac{R_{SH}}{1 + (W\tau)^2}$$

$$Z^{11} = \frac{W\tau R_{SH}}{1 + (W\tau)^2}$$

$$\text{TAN}\,\delta = \frac{Z^{11}}{Z^1} = \frac{W\tau R_{SH}}{R_{SH} + R_S\left[1 + (W\tau)^2\right]}$$

SYMBOL	MEANING
Z^*	COMPLEX IMPEDANCE
Z^1	STORAGE COMPONENT
Z^{11}	LOSS COMPONENT
i	$\sqrt{-1}$
τ	RELAXATION TIME
W	RADIAL FREQUENCY (RADIAN/SEC)
R_{SH}	SHUNT RESISTANCE
R_S	SERIES RESISTANCE
C	CAPACITANCE
I_L	LIGHT GENERATED CURRENT
I_D	DIODE LOSS CURRENT

SC80-9328

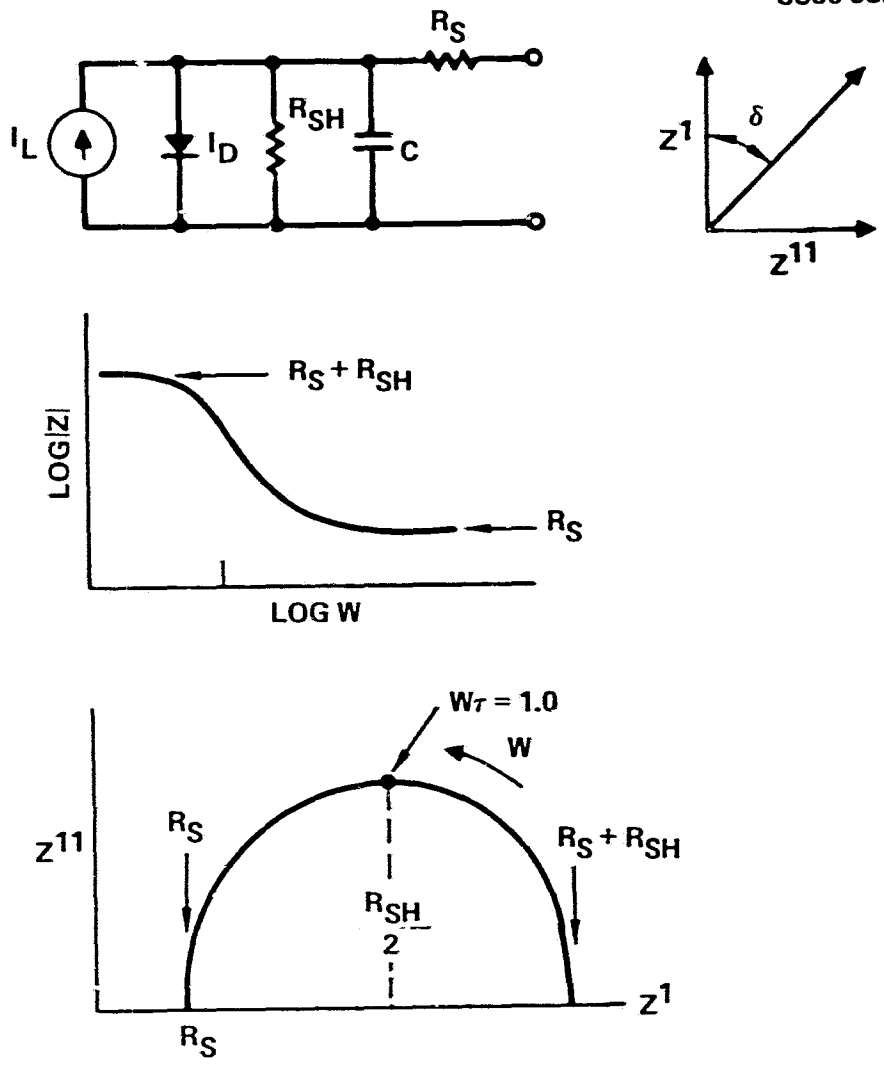

Fig. 5 Single cell AC impedance relations when $I_L = I_D = 0$.

Rockwell International
Science Center
SC5106.104AR

cumulative probability functions. The property mean value M_i and distribution shape factor m_i can be evaluated from measurements or theoretically assigned. This process for describing the statistical variability for a single cell can be repeated for each of the N cells making up the model branch circuit. The I-V response and AC impedance of each model cell can be calculated and combined in appropriate summation relations which describe the series-parallel cell interconnections in the branch circuit. Graphical illustrations for I-V summing in series-parallel networks are illustrated in Fig. 7. The methods by which particular types of defects can be located by I-V measurement of seperated portions of a branch circuit are graphically illustrated in Fig. 8.

4.2 Inpedance Model

The second portion of the analytical modeling effort has been directed at developing AC impedance as a nondestructive evaluation (NDE) tool for branch circuit analysis as a substitute for I-V characterization. Appendix II provides a detailed theoretical discussion and experimental appraisal of electrical impedance measurements and impedance spectum analysis of solar cells and elements of branch circuits. As pointed out in Appendix II, the new development of a simplified least squares circle fit of AC impedance data to a Cole-Cole distribution function provides an important augmentation of the methodology. This circular least-squares method is graphically illustrated in Fig. 9. A minimum of three AC data points with

WEIBULL DISTRIBUTIONS
P_i = CUMULATIVE PROBABILITY

INVERTED FUNCTIONS

SC81-11663

$P_1 = \exp\left[-(K_1/M_1)^{m_1}\right]$	$K_1 = M_1 \exp\left[\frac{1}{m_1} \ln(-\ln P_1)\right]$
$P_2 = \exp\left[-(K_2/M_2)^{m_2}\right]$	$K_2 = M_2 \exp\left[\frac{1}{m_2} \ln(-\ln P_2)\right]$
$P_3 = \exp\left[-(K_3/M_3)^{m_3}\right]$	$K_3 = M_3 \exp\left[\frac{1}{m_3} \ln(-\ln P_3)\right]$
$P_4 = \exp\left[-(I_D/M_4)^{m_4}\right]$	$I_D = M_4 \exp\left[\frac{1}{m_4} \ln(-\ln P_4)\right]$
$P_5 = \exp\left[-(V_D/M_5)^{m_5}\right]$	$V_D = M_5 \exp\left[\frac{1}{m_5} \ln(-\ln P_5)\right]$
$P_6 = \exp\left[-(R_S/M_6)^{m_6}\right]$	$R_S = M_6 \exp\left[\frac{1}{m_6} \ln(-\ln P_6)\right]$
$P_7 = \exp\left[-(R_{SH}/M_7)^{m_7}\right]$	$R_{SH} = M_7 \exp\left[\frac{1}{m_7} \ln(-\ln P_7)\right]$
$P_8 = \exp\left[-(C/M_8)^{m_8}\right]$	$C = M_8 \exp\left[\frac{1}{m_8} \ln(-\ln P_8)\right]$

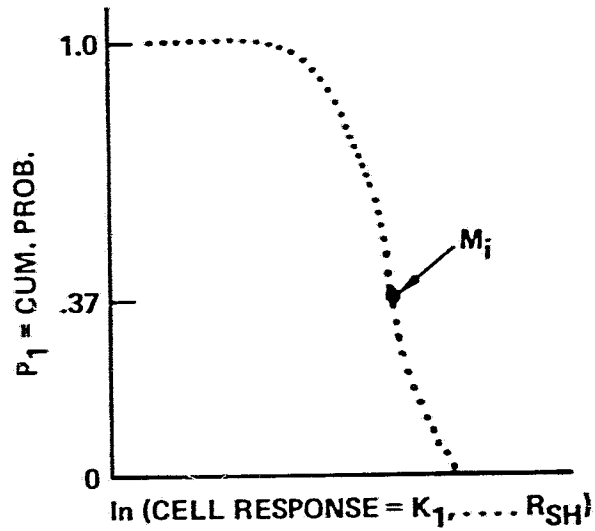

1) DEFINE TOTAL NUMBER OF CELLS N
2) DEFINE DISCRETE VALUES OF $P_i = \frac{J-0.50}{N}$ FOR J = 1, 2, 3 . . . . N
3) DEFINE M_i AND m_i FOR i = 1, 2, 3 . . . 8
4) GENERATE A RANDOM NUMBER BETWEEN ZERO AND ONE
5) SET RANDOM NUMBER EQUAL TO CLOSEST VALUE OF P_i
6) SOLVE INVERTED FUNCTION FOR CELL RESPONSE IN TERMS OF P_i, M_i, AND m_i FOR i = 1
7) REPEAT STEPS (4) TO (6) FOR PROPERTIES i = 2 TO 8

Fig. 6 Statistical variability of single cell I-V responses.

- FOR ELEMENTS IN SERIES ADD VOLTAGES ALONG CONSTANT CURRENT LINES

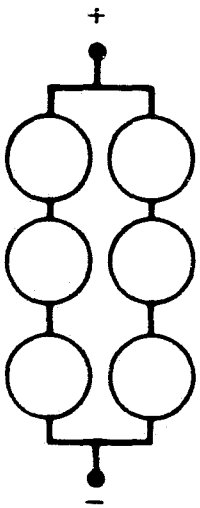

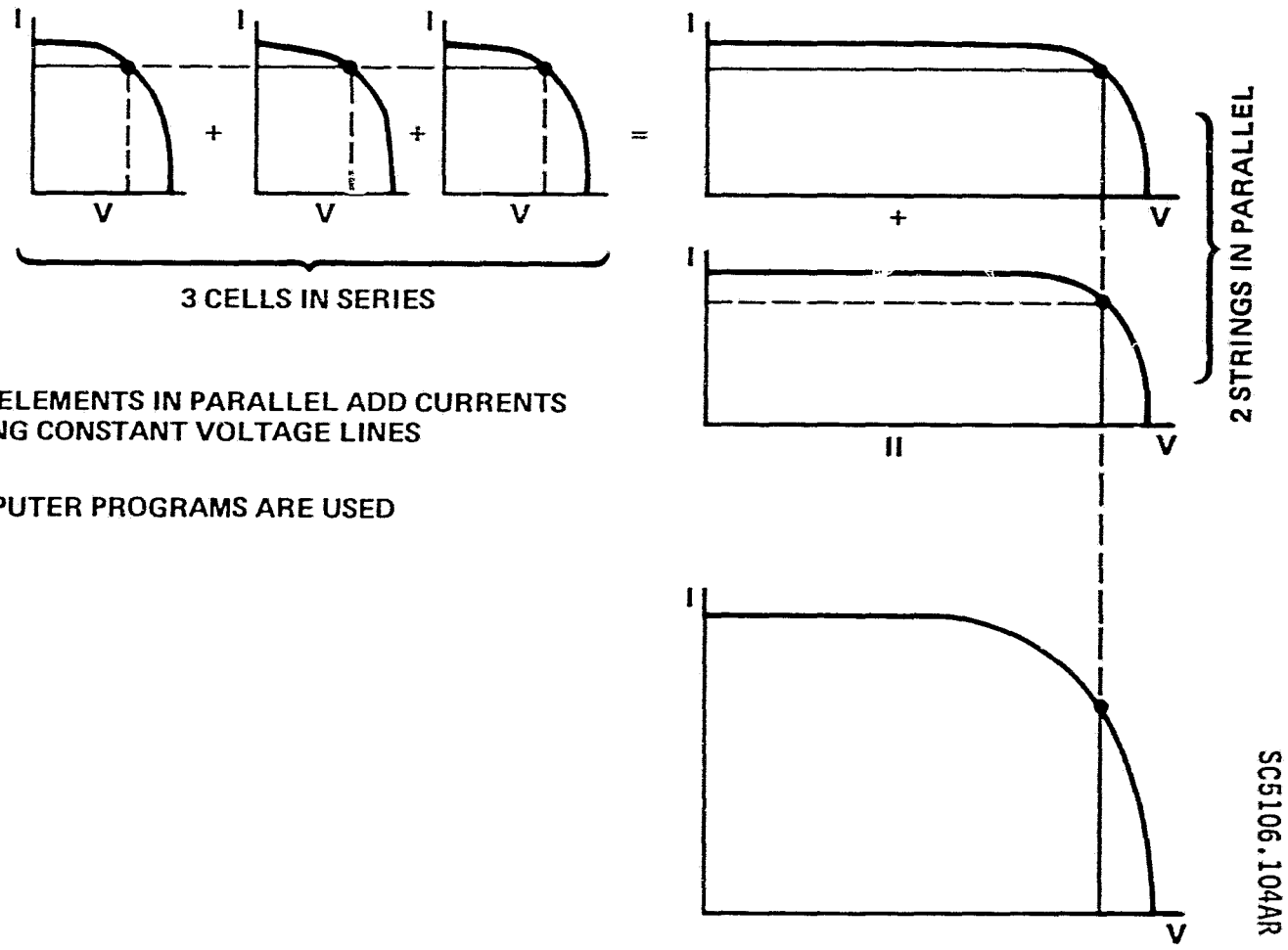

- FOR ELEMENTS IN PARALLEL ADD CURRENTS ALONG CONSTANT VOLTAGE LINES
- COMPUTER PROGRAMS ARE USED

Fig. 7 I-V curve calculation for series parallel networks (from Ref. 6).

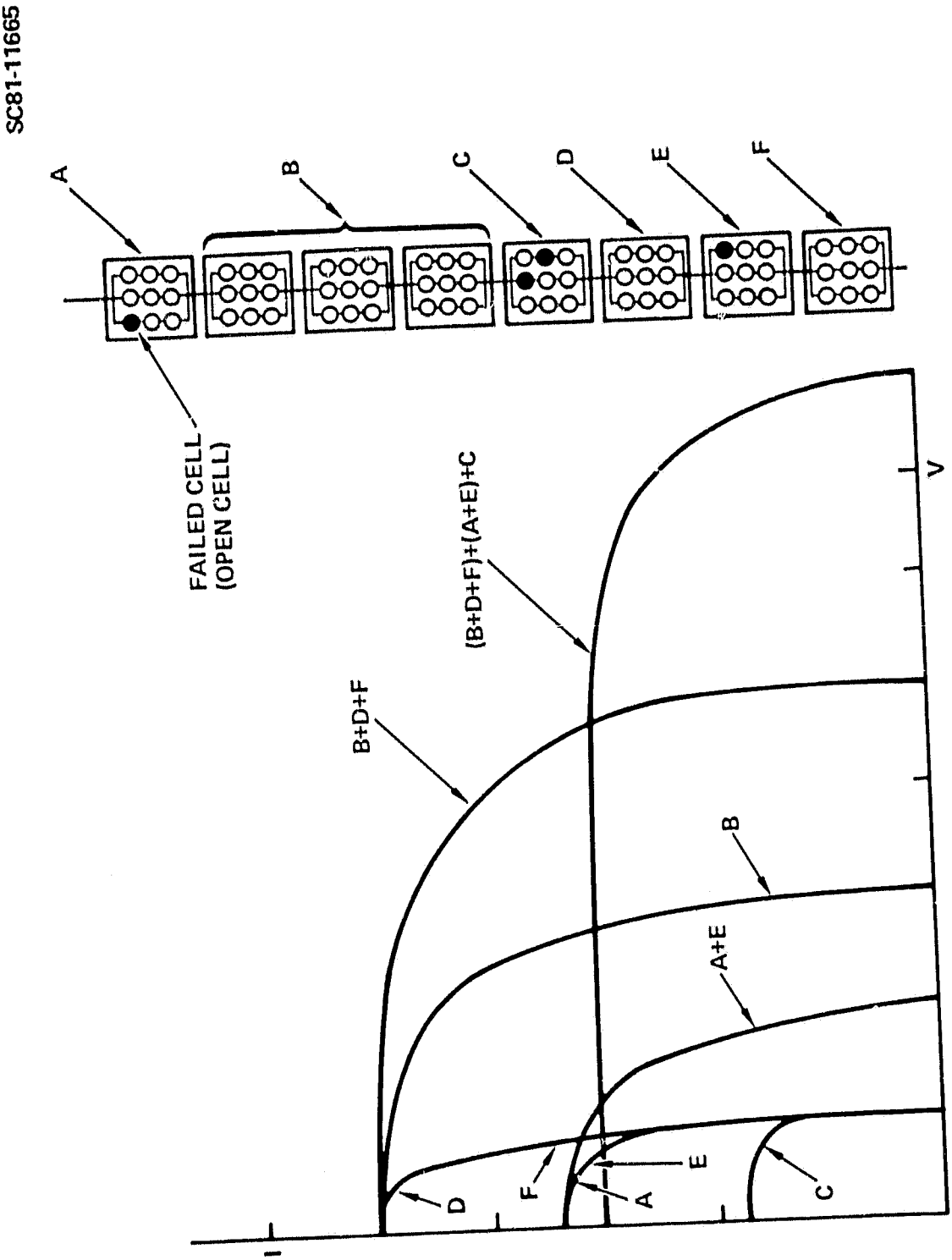

Fig. 8 Simulation of cumulative I-V curve for a branch circuit containing failed and unfailed elements.

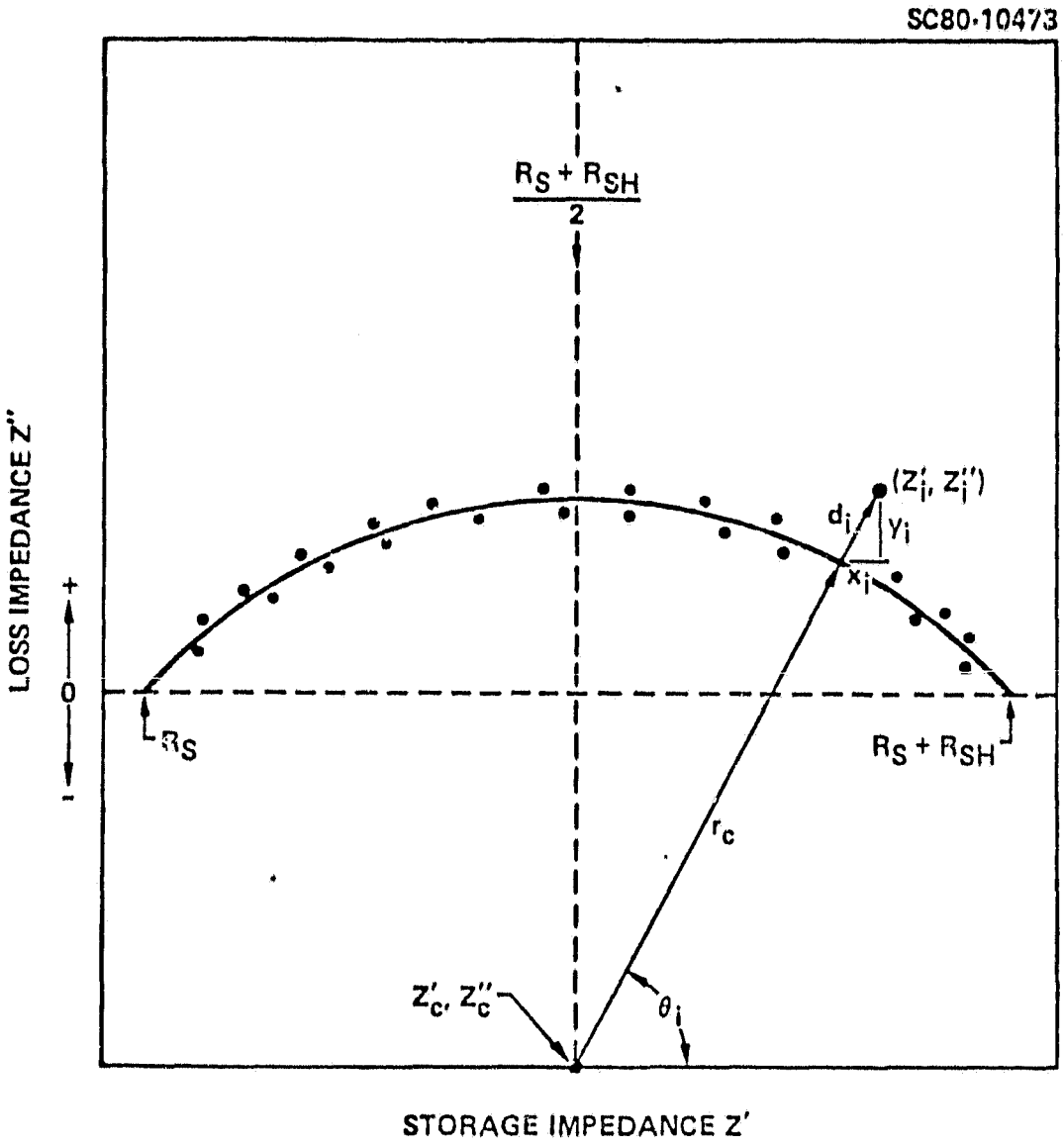

Fig. 9 Schematic representation of least squares circle fit of the Cole-Cole AC impedance funciton.

sufficient seperation on the Z" vs Z' coordinates of Fig. 9 are sufficient to determine the values of R_S and R_{SH} and the distribution quality factor $0<\beta<1.0$ for multiple interconnected solar cells. If all the cells have identical impedance response then $\beta=1.0$. As Appendix II shows, the mismatch of AC impedance response tends to lower β and at the same time produce mismatches in I-V responses between cells which lower photovoltaic performance.

The potential simplicity of AC impedance measurement and spectrum analysis as outlined in Appendix II suggest the potential of remote impedance, monitoring and feedback control of a solar array branch circuit. A preliminary model for AC impedance measurement, impedance spectrum analysis, and feedback control to an LSA branch circuit is graphically outlined in Fig. 10. In brief, the solar array branch circuit is viewed as equipped with digitally controlled series-parallel interconnects between modules. AC impedance measurements conducted at the solar array site would be digitized and transmitted to a control location of impedance spectrum analysis. An analytical branch circuit IV (current-voltage) model and predicted impedance spectrum would be incorporated in a corrective action analysis. Corrective action could be transmitted to the power control (PC) unit at the solar array site by digital encoded instructions that modify the series to parallel (S/P) interconnects in the solar array. The modified S/P interconnection can be utilized to locate deteriorated modules and to reoptimize the branch circuit electrical outputs for maximum power output.

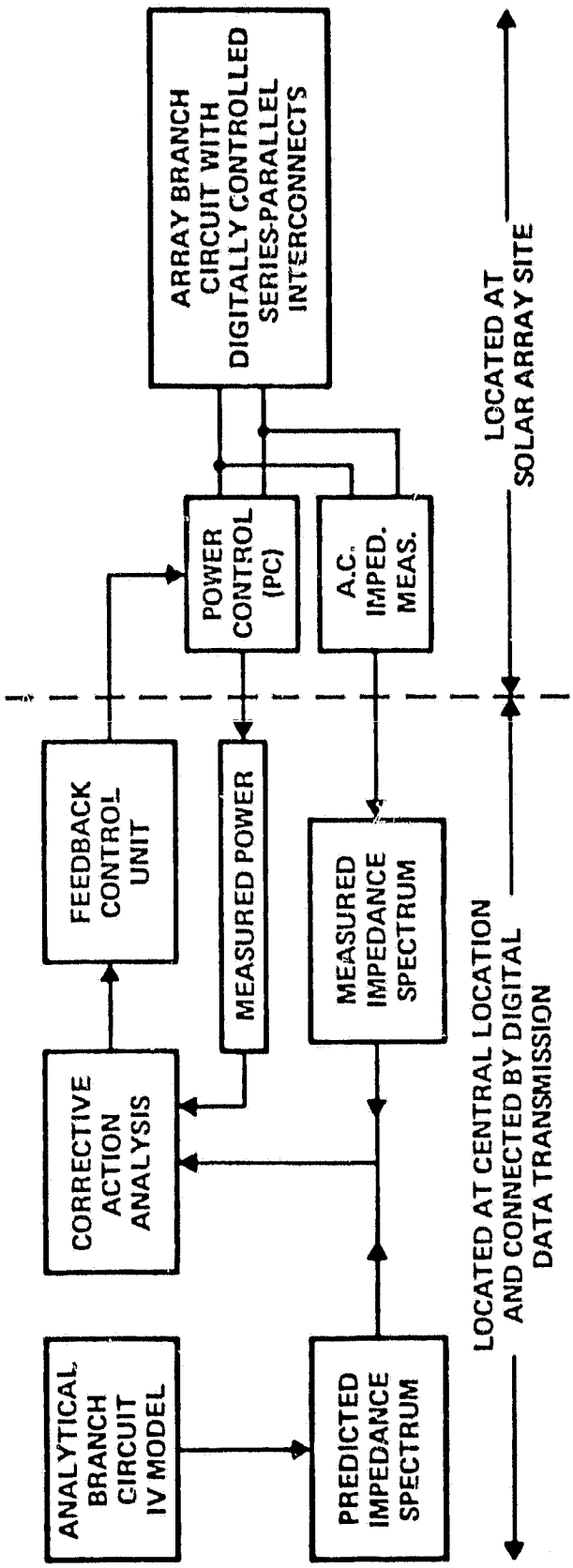

Fig. 10 Block diagram of an AC impedance measurement, spectrum analysis, and feedback switching control for a solar array branch circuit.

AC impedance is viewed as a method for augmenting power output measurement to provide highly sensitive and interpretable data on environmental aging effects. The interpretation and control methodology outlined above would integrate nondestructive evaluation (NDE) with a corrective action program to locate and minimize environmental aging effects on array performance.

5.0 EXPERIMENTAL

This section discusses and interrelates the results of natural corrosion studies at the Mead test site and computer modeling and accelerated aging at the Science Center.

5.1 Mead Site Atmospheric Corrosion Monitoring

As reported in the third annual report (SC5106.86AR), a new atmospheric corrosion model, as outlined in Fig. 11 was developed and implemented in corrosion studies at the Mead test site. As shown in Fig. 11, the corrosion rate is predicted to be the product of the surface condensation probability of water vapor P_C and the diffusion controlled corrosion current I_L. This model combines surface physical chemistry and electrochemisty and is verified by the direct correlation between relative humidity and the logarithm of measured corrosion current as shown in the upper right view of Fig. 11.

The corrosion monitor experiment was initiated at Mead, Nebraska on July 12, 1979 and continued for over a year until terminated in October 1980. A photographic view of the Mead, Nebraska LSA test site is shown in the upper view of Fig. 12. The lower view of Fig. 12 shows two atmospheric corrosion monitors (ACM) installed on the right rear portion of the array. The monitors consist of the edges of alternating plates of Zn and Cu seperated by a 50 μm polyester (DuPont-Mylar) dielectric film. Moisture condensation on the exposed surface closes the circuit between the plates and current flows.[10] The solid state circuitry of the ACM converts the logarithm of the current

COMBINED CONDENSATION DIFFUSION

$$I = P_c \frac{nFDC}{\delta t}$$

$$P_c = \exp\left[\frac{-1.756\ 10^{22}\ \phi\ v^2\ \gamma_{LV}^3}{T^3\ (\ln P/P_o)^2}\right]$$

SURFACE ENERGY EFFECTS

$$\phi = 0.25\left[2 + \cos^3\theta - 3\cos\theta\right]$$

$$\cos\theta = \frac{2\left[\alpha_L\alpha_S + \beta_L\beta_S\right]}{\gamma_{LV}} - 1 < 1.0$$

SURFACE ROUGHNESS

$$T_r = T + \Delta T$$

$$\Delta T = \frac{-2\ \gamma_{LV}\ T_o}{\Delta H_V\ r_c}$$

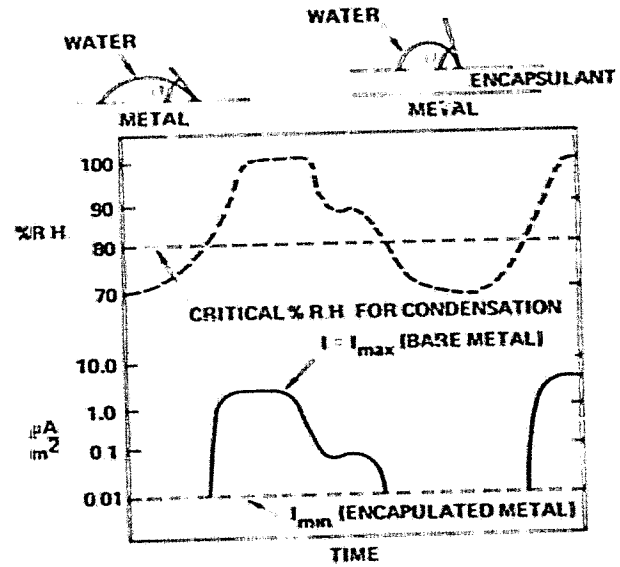

ELECTROCHEMISTRY

- I CORROSION CURRENT DENSITY (Amp/m^2)
- P_c CONDENSATION PROBABILITY
- n NUMBER OF ELECTRONS
- D DIFFUSION COEFFICIENT OF REDUCING ION
- F FARADAY (96500 COULOMBS/EQUIVALENT
- C CONCENTRATION OF DIFFUSING IONS
- δ THICKNESS OF DIFFUSION LAYER ($\cong 5 \times 10^{-4}$m IN STATIC SOLUTION)
- t TRANSFER NUMBER OF ALL IONS IN SOLUTION ($\cong$1.0 IF MANY IONS PRESENT)

CONDENSATION

- v WATER MOLAR VOLUME
- P WATER VAPOR PRESSURES
- P_o WATER SATURATION VAPOR PRESSURE

SURFACE ENERGY

- ϕ WETTABILITY FUNCTION
- θ WATER SOLID CONTACT ANGLE
- γ_{LV} WATER SURFACE TENSION
- $\alpha_L\beta_S$ RESPECTIVE DISPERSION AND POLAR SURFACE PROPERTIES OF WATER
- $\alpha_S\beta_S$ RESPECTIVE DISPERSION AND POLAR SURFACE PROPERTIES OF SOLID SURFACE

SURFACE CAPILLARITY

- T AMBIENT KELVIN TEMPERATURE
- T_r REDUCED TEMPERATURE FOR CAPILLARY CONDENSATION
- T_o TEMPERATURE FOR VAPOR SATURATION
- ΔH_V WATER HEAT OF VAPORIZATION
- r_c SURFACE CAPILLARY RADIUS

Fig. 11 Atmospheric corrosion model.

SC80-10059

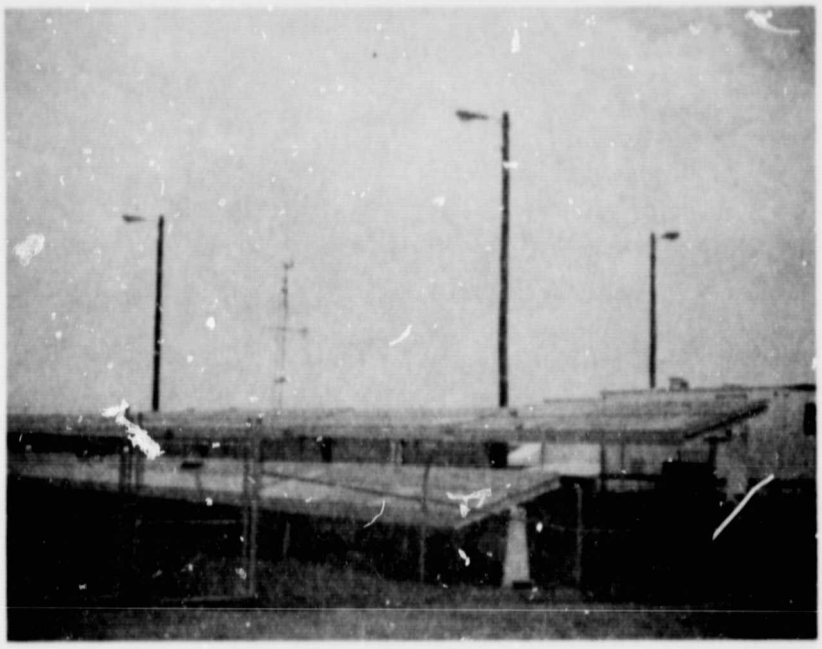

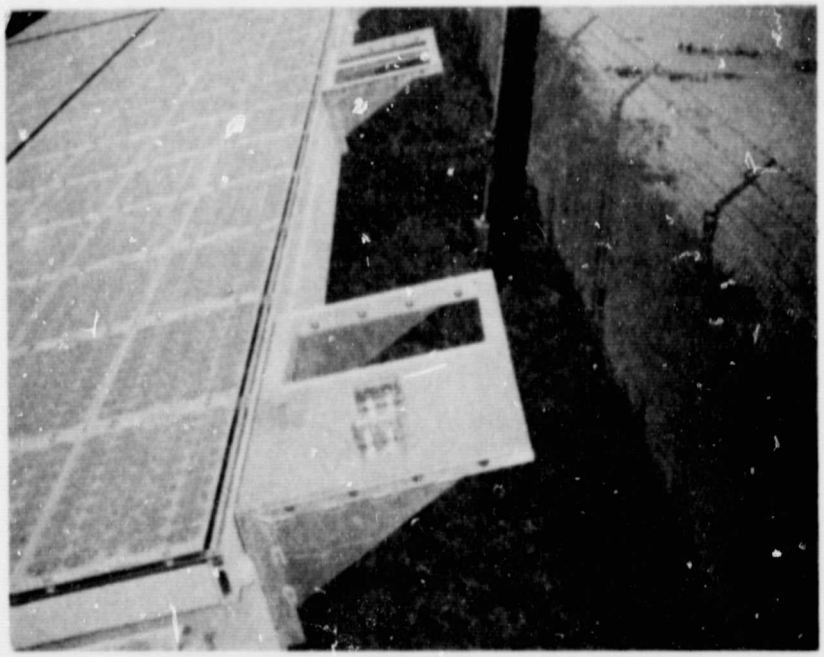

Fig. 12 Photographic view of Mead, Nebraska LSA test site (upper view) and atmospheric corrosion monitors (lower view) installed on rear right portion of array.

(microamperes) to a proportional DC voltage which is transmicted to the recording station located in the power control unit (PCU) located behind the right end of the array (see upper view Fig. 12). Specific details of the corrosion and climatology recordings are discussed in the third annual report (SC5106.86AR).

During the 13 month deployment at the Mead, Nebraska test site the ACM units recorded, at 10 minute intervals, the corrosion protection function of an encapsulant system consisting of a reactive primer, General Electric GE-SS4155, on Zn/Cu plates encapsulated by 2mm of Dow Sylgard 184 silicone. A non-encapsulated ACM unit correlated Mead climatology with corrosion rates as defined by the atmospheric corrosion model outlined in Fig. 11.

The fundamental assumptions of the corrosion model appear verified in this 13 month study. As shown in the upper curves Fig. 13 and Fig. 14 the encapsulated ACM showed a negligible corrosion rate under both wet and dry conditions during the entire 13 month exposure period. The nonencapsulated ACM unit showed a linear interrelation between the logarithm of corrosion current I and moisture supersaturation temperature (T_D-T) (dew point minus temperature) as defined by the corrosion model. Below a critical relative humidity or (T_D-T) for surface condensation the condensation probability P_c is negligible and corrosion current is minimized to the lower limits of current detection. During periods of surface condensation the uncoated ACM achieves a maximum current output which is the diffusion controlled current I_L. The negligible current of the encapsulated ACM identifies the mechanism of encapsulant corrosion protection as specifically related to the suppression of I_L at the potential corroding interface.

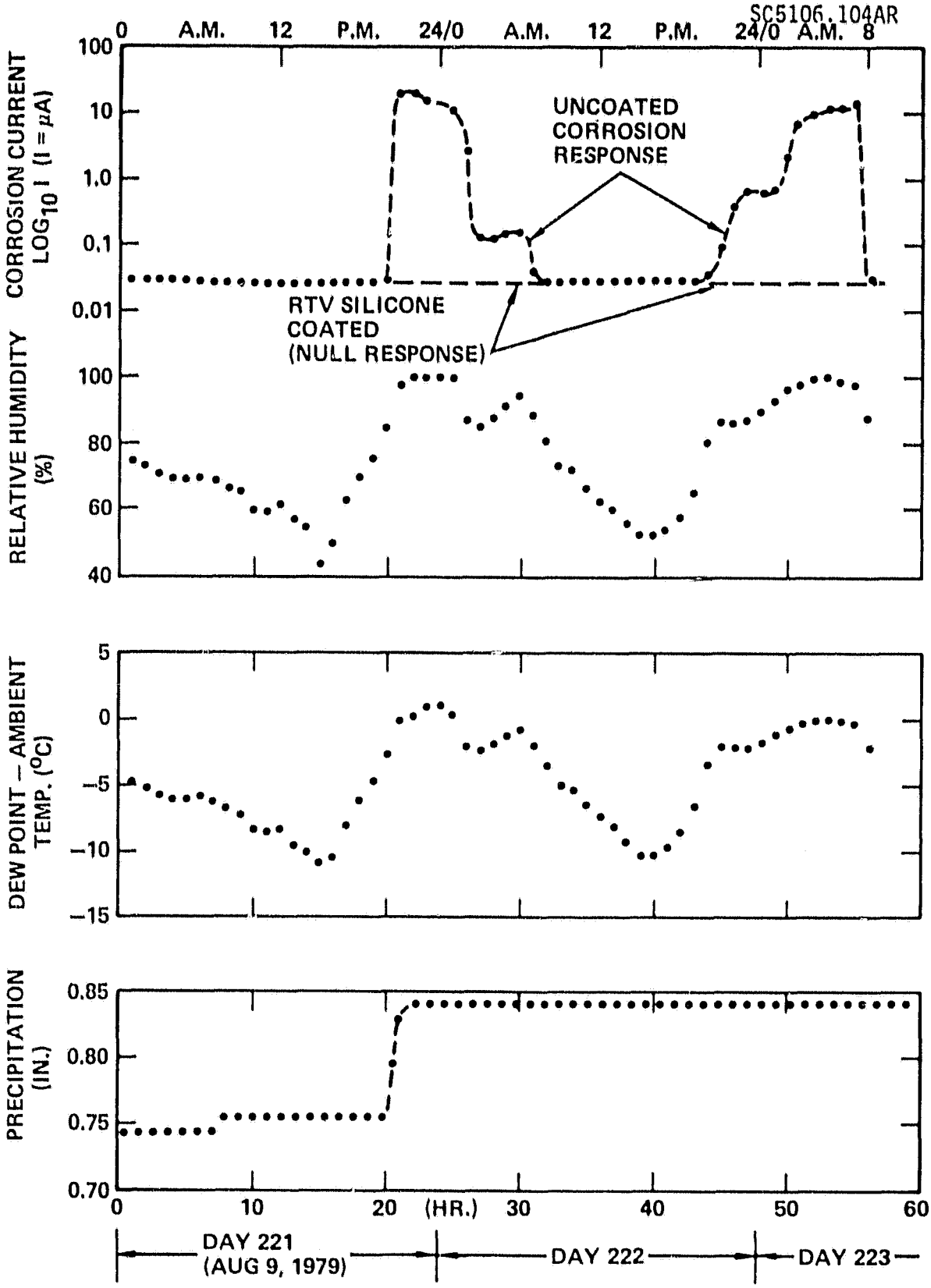

Fig. 13 Corrosion monitor (upper view) correlation to Mead site moisture and rain climatology after 28 days exposure.

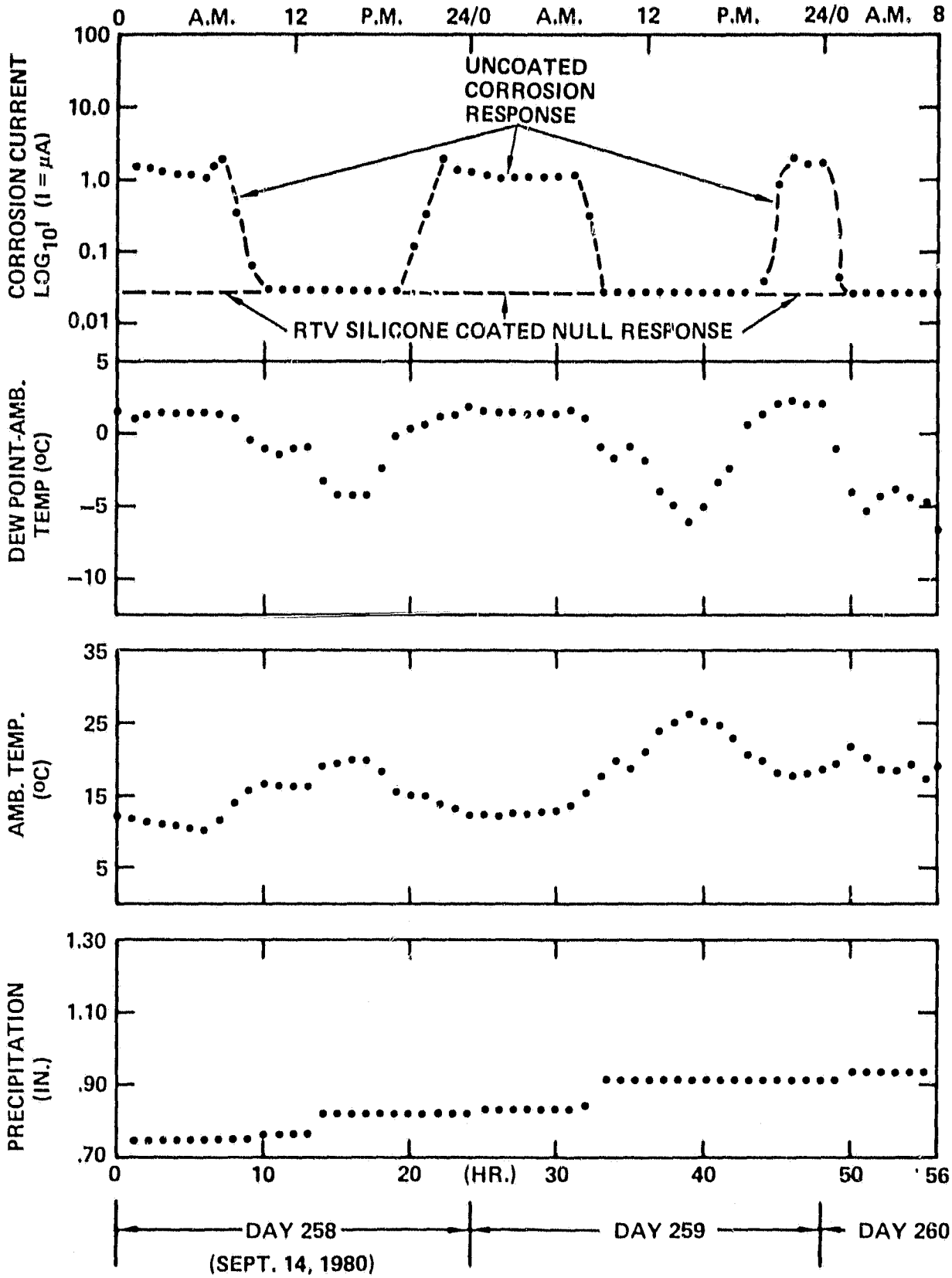

Fig. 14 Corrosion monitor (upper view) correlation to Mead site moisture and rain climotology after 429 days exposure.

Outdoor aging effects on the maximum corrosion current at 100% R. H. of the uncoated ACM are shown in Fig. 15. This maximum current displays weekly and seasonal variability which depends upon the ionic conductivity of surface film produced by both corrosion and dirt accumulation. The upper curve of Fig. 15 points out that this maximum current decreases from ≈ 20 μA for an unaged ACM to ≈5 μA after 13 months exposure. As previously documented,[11] and shown in Fig. 15, the freeze-thaw cycles of Mead winter cause a wide variability in maximum current due to lowered diffusion and ion solubility in ice as opposed to water.

The curves of Fig. 16 clearly show the effects of Mead aging by plotting the logarithm of corrosion current I versus moisture supersaturation temperature ($\bar{T}_D - \bar{T}$). These plots are obtained by parametric cross plotting the respective I and ($T_D - T$) data of Fig. 13 and Fig. 14 at equivalent time conditions. The upper curve of Fig. 16 shows a lower limit corrosion current I ≈0.04 μA characteristic of the lower limit of measurement sensitivity. At this lower limiting current the dry uncoated and encapsulated ACM are equivalent in response. As shown in Fig. 16 with increasing supersaturation temperatures ($T_D - T$) the corrosion current displaces to an upper limit characteristic of diffusion controlled response. Referring to the corrosion model (see Fig. 11) the transition region for corrosion current output is related to water wettability and capillary absorption. The curves of Fig. 16 show that this transition region is significantly shifted to higher values of $T_D - T$ as a consequency of Mead outdoor exposure. The same aging factors which tend to lower maximum current, such as film formation and contamination, can be expected to diminish water wettability and capillarity.

SC81-11662

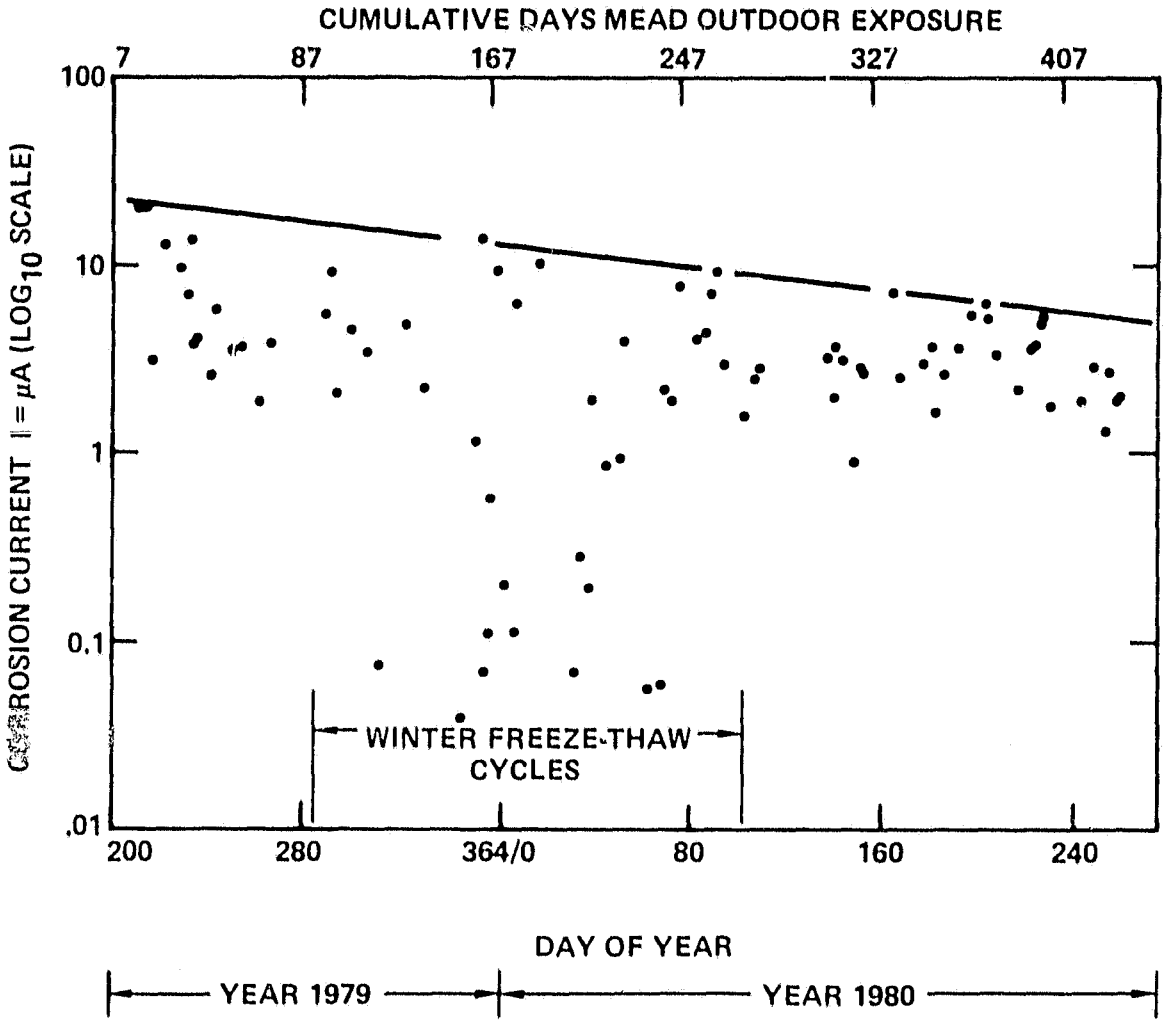

Fig. 15 Maximum atmospheric corrosion monitor (ACM) current I at 100% relative humidity versus Mead site exposure time (days).

SC81-11666

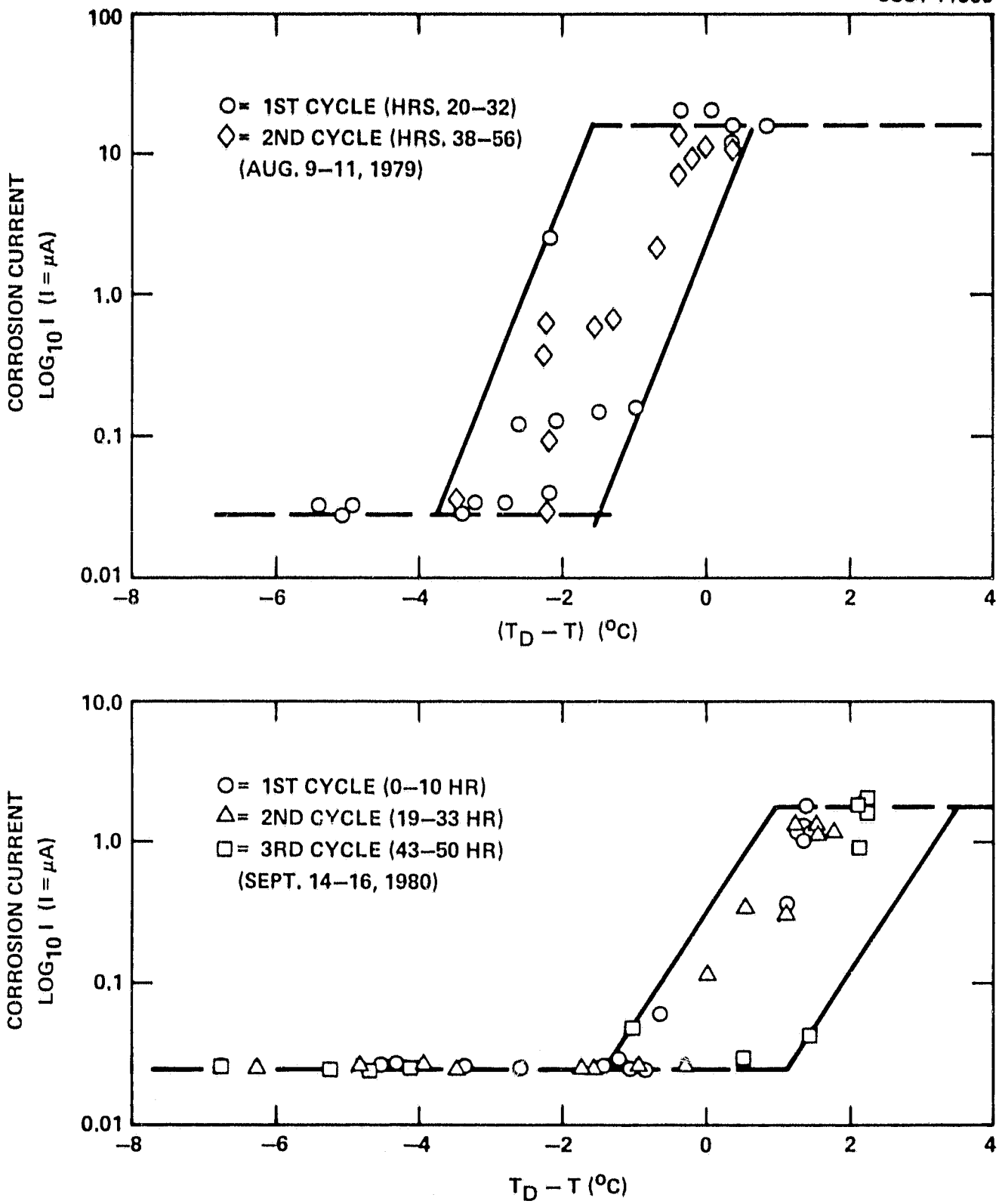

Fig. 16 Corrosion monitor current (I) vs. moisture super saturation temperature (T_D-T) at 28 days (upper view) and 429 days (lower view) outdoor Mead exposure.

Photographic views of the uncoated and encapsulated ACM units subsequent to 430 days Mead outdoor exposure are shown in Fig. 17. The uncoated ACM shows ample evidence of extensive corrosion and material erosion while the encapsulated ACM shows the original metallic luster and intact interfacial bond to encapsulant characteristic of complete corrosion suppression at the Cu/Zn plate surface. Based upon these results the GE-SS4155 reactive primer appears as a strong condidate in planned studies of interface corrosion durability.

5.2 Hydrothermal Stress Analysis

An earlier environmental study by E. Laue and A. Gupta at JPL[12] showed that combined moisture and UV cycling of an EVA (ethylene vinylacetate) encapsulated silicon solar cell on a wood composite substrate produced cell cracking and evidence of subsequent microcrack corrosion. The Science Center had recently completed development of a hyrothermal stress analysis (HTSA) program for composite laminates[7] and a study was undertaken to explore the applications of the HTSA model in LSA life prediction. The logic flow chart for the HTSA model is shown in Fig. 18. As shown in Fig. 18 the HTSA model imputs a physical description of layers, the hydrothermal, and mechanical properties of each layer, and the discription of the hydrothermal cycles imposed in the simulated aging study.

A cross section of the solar cell laminate considered for HTSA modeling is shown in the upper view of Fig. 19. Where the cell front surface faces right. The combined variations in temperature and humidity are shown in

SC81-12330

Fig. 17 Uncoated (left) and encapsulated (right) corrosion monitors after 430 days outdoor exposure at Mead, Nebraska test site.

SC80-9333

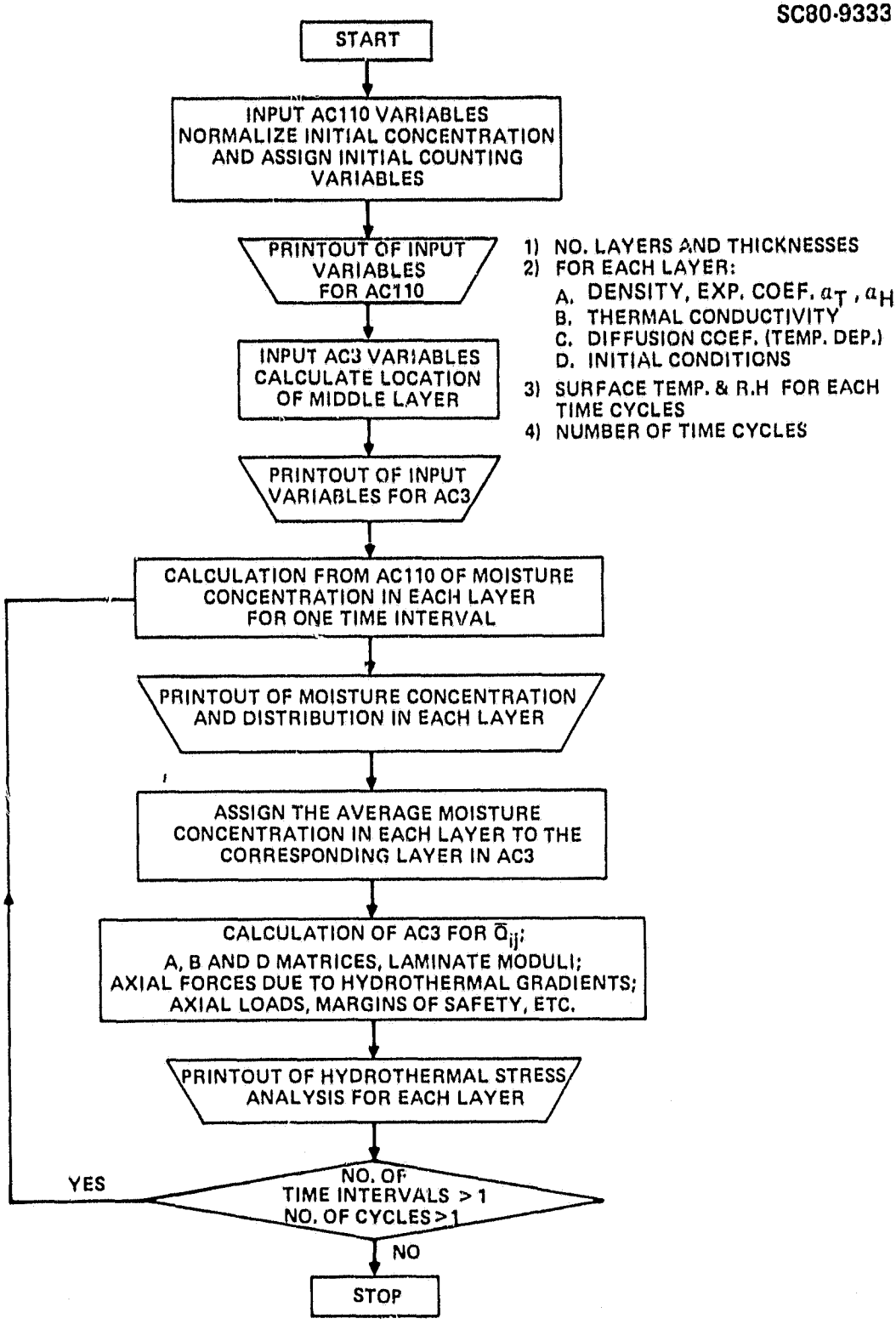

Fig. 18 Flowchart of hydrothermal stress analysis program.

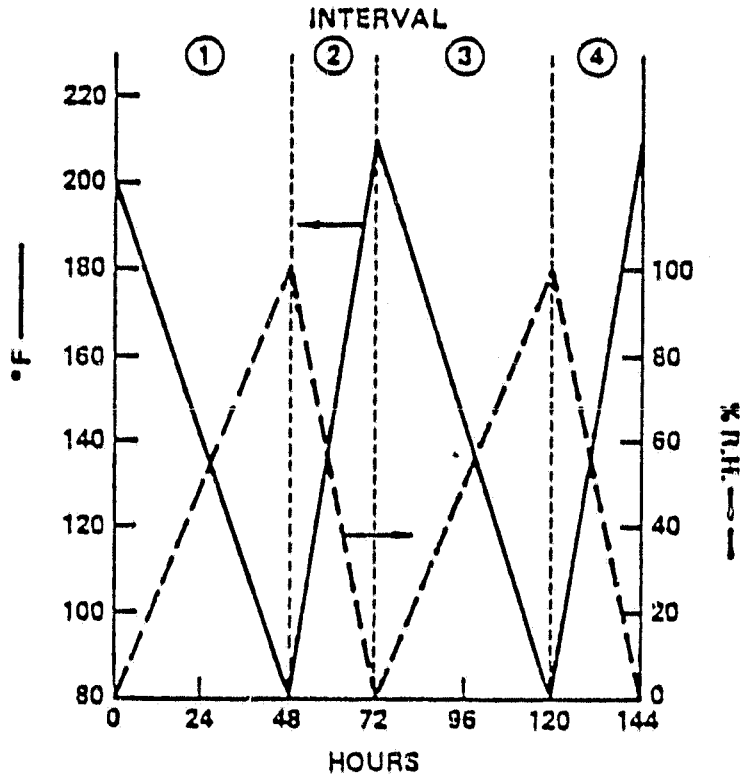

Fig. 19 Hydrothermal history of one environmental exposure cycle.

the lower curves of Fig. 19. The first computer run did not include layer 5 which represents a moisture diffusion barrier film on the back surface of the solar cell.

Moisture diffusion properties for both clear and pigmented EVA encapsulant films obtained from JPL were experimentally determined and these properties are reported in Table 1. The full temperature dependent moisture and thermal diffusion imputs for each of the four solar cell layers (see Fig. 19) which are input to the HTSA model are summarized in Table 2. The hydro-thermal-elastic coefficients for the four solar cell layers for HTSA input are detailed in Table 3.

The computed moisture and stress profiles produced by the end of first 48 hours interval of hydration for the four layer laminate is shown upper Fig. 20. The moisture is seen to penetrate both layer 1 and 4 and to produce a substantial biaxial tensile stress in the silicon wafer which is counterbalanced by a lower biaxial compressive stress in the fiber board. Encapsulant layers 1 and 3 show minor biaxial tension at this point.

The lower view of Fig. 20 shows the moisture and stress profiles at the end of the 24 hr drying cycle which forms the second interval of aging. All the moisture in layer 1 is essentially removed but only the surface moisture is lowered in the thicker fiber board layer 4. Both the tensile stresses in the silicon layer 2 and compressive stress in layer 4 are slightly diminished by this drying cycle. An interesting and important feature of interlaminal cracking in the fiber board layer 4 is shown in the steep moisture

Table 1 Moisture Diffusion Properties of Solar Cell Encapsulants
Diffusion Equation $D = D_o \exp(-E_D/RT)$

Moisture diffusion coeff. at 22°C, (mm^2/sec)	5×10^{-7}	1×10^{-7}
Max. H_2O uptake at 100% RH R-T	0.08%	0.3%
Activation energy, E_D, Kcal/mole	12	13
D_o (mm^2/sec)	316	370

Table 2 Moisture Diffusion Input to HTSA Model (4 Layers, Fig. 19)

```
NUMBERS OF LAYERS = 4
THE PLATE IS EXPOSED ON BOTH SIDES.


INITIAL COCENTRATION DISTRIBUTION

LAYER 1 C(0/0) AT X(IN)
X     .0000     .0045     .0095     .0143     .0190
C     .0000     .0000     .0000     .0000     .0000

LAYER 2 C(0/0) AT X(IN)
X     .0000     .0047     .0095     .0143     .0190
C     .0000     .0000     .0000     .0000     .0000

LAYER 3 C(0/0) AT X(IN)
X     .0000     .0047     .0095     .0143     .0190
C     .0000     .0000     .0000     .0000     .0000

LAYER 4 C(0/0) AT X(IN)
X     .0000     .0313     .0625     .0938     .1250
C     .0000     .0000     .0000     .0000     .0000

LAYER 1
LAYER THICKNESS       H = .0190 INCHES
THERMAL CONDUCTIVITY =   .15000 BTU/(HR-FT-F)
DENSITY =   57.00000LBM/(FT**3)
FOR TEMPERATURE LESS THAN    .0 DEGREE C       D =   .200E-02EXP(   -3000.0/TEMP.)  MM**2/SEC.
FOR TEMPERATURE GREATER THAN    .0 DEGREE C    D =   .570E 00EXP(   -5000.0/TEMP.)  MM**2/SEC
TEMP. IS IN DEGREE K
BOUNDARY CONCENTRATION IS GIVEN BY EQUATION    C =   .001500 *HUM.** 1.00
LAYER 2
LAYER THICKNESS       H = .0190 INCHES
THERMAL CONDUCTIVITY =  1.00000 BTU/(HR-FT-F)
DENSITY =  144.00000LBM/(FT**3)
FOR TEMPERATURE LESS THAN    .0 DEGREE C       D =   .100E-04EXP(  -500000.0/TEMP.)  MM**2/SEC.
FOR TEMPERATURE GREATER THAN    .0 DEGREE C    D =   .570E 00EXP(    -5000.0/TEMP.)  MM**2/SEC.
TEMP. IS IN DEGREE K

BOUNDARY CONCENTRATION IS GIVEN BY EQUATION    C =   .00000 *HUM.** 1.00
LAYER 3
LAYER THICKNESS     H =  .0190 INCHES
THERMAL CONDUCTIVITY =   .15000 BTU/(HR-FT-F)
DENSITY =   57.00000LBM/FT**3)
FOR TEMPERATURE LESS THAN     .0 DEGREE C      D =   .200E-02EXP(    -3000.0/TEMP.)  MM**2/SEC.
FOR TEMPERATURE GREATER THAN  .0 DEGREE C      D =   .570E 00EXP(    -5000.0/TEMP.)  MM**2/SEC.
TEMP. IS IN DEGREE K
BOUNDARY CONCENTRATION IS GIVEN BY EQUATION    C =   .003000 *HUM.** 1.00
```

Table 2 (continued)

LAYER 4
LAYER THICKNESS H = .1250 INCHES
THERMAL CONDUCTIVITY = .33000 BTU/(HR-FT-F)
DENSITY = 72.00000LBM/(FT**3)
FOR TEMPERATURE LESS THAN .0 DEGREE C D = .200E-01EXP(-16000.0/TEMP.) MM**2/SEC.
FOR TEMPERATURE GREATER THAN .0 DEGREE C D = .570E 00EXP(-5000.0/TEMP.) MM**2/SEC.
TEMP. IS IN DEGREE K

BOUNDARY CONCENTRATION IS GIVEN BY EQUATION C = .250000 *HUM.** 1.00

TIME HOUR	START LEFT T	START RIGHT T	FINAL LEFT T	FINAL RIGHT T	START LEFT H	START RIGHT H	FINAL LEFT H	FINAL RIGHT H
.0 TO 48.0	212.0	212.0	80.0	80.0	.0	.0	100.0	100.0
48.0 TO 72.0	80.0	80.0	212.0	212.0	100.0	100.0	.0	.0
72.0 TO 120.0	212.0	212.0	80.0	80.0	.0	.0	100.0	100.0
120.0 TO 144.0	80.0	80.0	212.0	212.0	100.0	100.0	XXX.0	XXX.0

NUMBER OF CYCLES 10

Table 3 Hydro-Thermal-Elastic Imput to HTSA Model (4 Layers, Fig. 19)

```
                    POINT STRESS ANALYSIS
        (REFERENCE CH. 2.1 OF THE ADVANCED COMPOSITE DESIGN GUIDE - THIRD ED.)

              INPUT DATA                                                    NOMENCLATURE
        NL = 4     NM = 4     NS = 1              NLD = 1                  NL = NO. LAYERS
             PRINT DATA FOR LAYERS 1, 4, 1                                NM = NO. MATERIALS
             THE STRESS FAILURE CRITERIA IS USED                          NS = NO. SETS
                                                                         NLD = NO. LOAD CONDITIONS
        MATERIAL 1 IS CLEAR EVA                                           E = YOUNGS MODULUS
                                                                          U = POISSONS RATIO
 E(L) =   20000.    E(T) =   20000.    G(LT) =   600.     ALPHW(L) = .0000800   ALPHA=COEF THERMAL EXPANSION
U(LT) =  .5000  ALPHA(L) = .0002000 ALPHA(T) =  .0002000  ALPHW(T) = .0000800  EPS=AXIAL STRAIN
        DEFAULTS       TAU =    .0   THICKNESS =  .0200                      CHI=ROTATIONAL STRAIN

SIGA(L) =  1890.  SIGA(T) =  1890.   SIGA(LT) =     110.
SIGA(L) = -1890.  SIGA(T) = -1890.                              N,M,Q=AXIAL, MOMENT, SHEAR LOAD

             MATERIAL 2 IS SILICON
 E(L) = 24000000.     E(T) =  24000000.   G(LT) = 10000000.   ALPHW(L) = .0000010
U(LT) =  .2100    ALPHA(L) =  .0000020 ALPHA(T) = .0000020   ALPHW(T) = .0000010
       DEFAULTS        TAU =     .0   THICKNESS = .0200

SIGA(L) =  40000.   SIGA(T) =  40000.   SIGA(LT) =  10000.
SIGA(L) = -40000.   SIGA(T) = -40000.                           N,M,Q=AXIAL, MOMENT, SHEAR LOAD

             MATERIAL 3 IS EVA WHITE
 E(L) = 20000.        E(T) =  20000.       G(LT) =  600        ALPHW(L) = .0000800
U(LT) = .5000   ALPHA)L) =  .0002000   ALPHA(T) =  .0002000   ALPHW(T) = .0000800
       DEFAULTS        TAU =      .0    THICKNESS = .0200

SIGA(L) =  1710.     SIGA(T) =  1710.     SIGA(LT) =  110.
SIGA(L) = -1710.     SIGA(T) = -1710.                           N,M,Q=AXIAL, MOMENT, SHEAR LOAD

             MATERIAL 4 IS FIBERBOARD
 E(L) =  900000.      E(T) =  900000.      G(LT) =  300000.   ALPHW(L) = .0063000
U(LT) = .3000   ALPHA(L) =  .0000040     G(LT) =  .0000040  ALPHW(L) = .0063000
       DEFAULTS        TAU =      .0    THICKNESS = .1250

SIGA(L) =  4430.     SIGA(T) =  4430.     SIGA(LT) =  2860.          N,M,Q=AXIAL, MOMENT, SHEAR LOAD
SIGA(L) = -4620.     SIGA(T) = -4620.

                                                                    NT,MT=*N,M*DUE TO TAU
                                                                       TAU=TEMPERATURE DIFFERENTIAL
                                                                        SIG = APPLIED STRESS
                                                                      EPSA = ALLOWABLE STRAIN
                                                                      SIGA = ALLOWABLE STRESS
                                                                    SIGBAR = AVERAGE STRESS
```

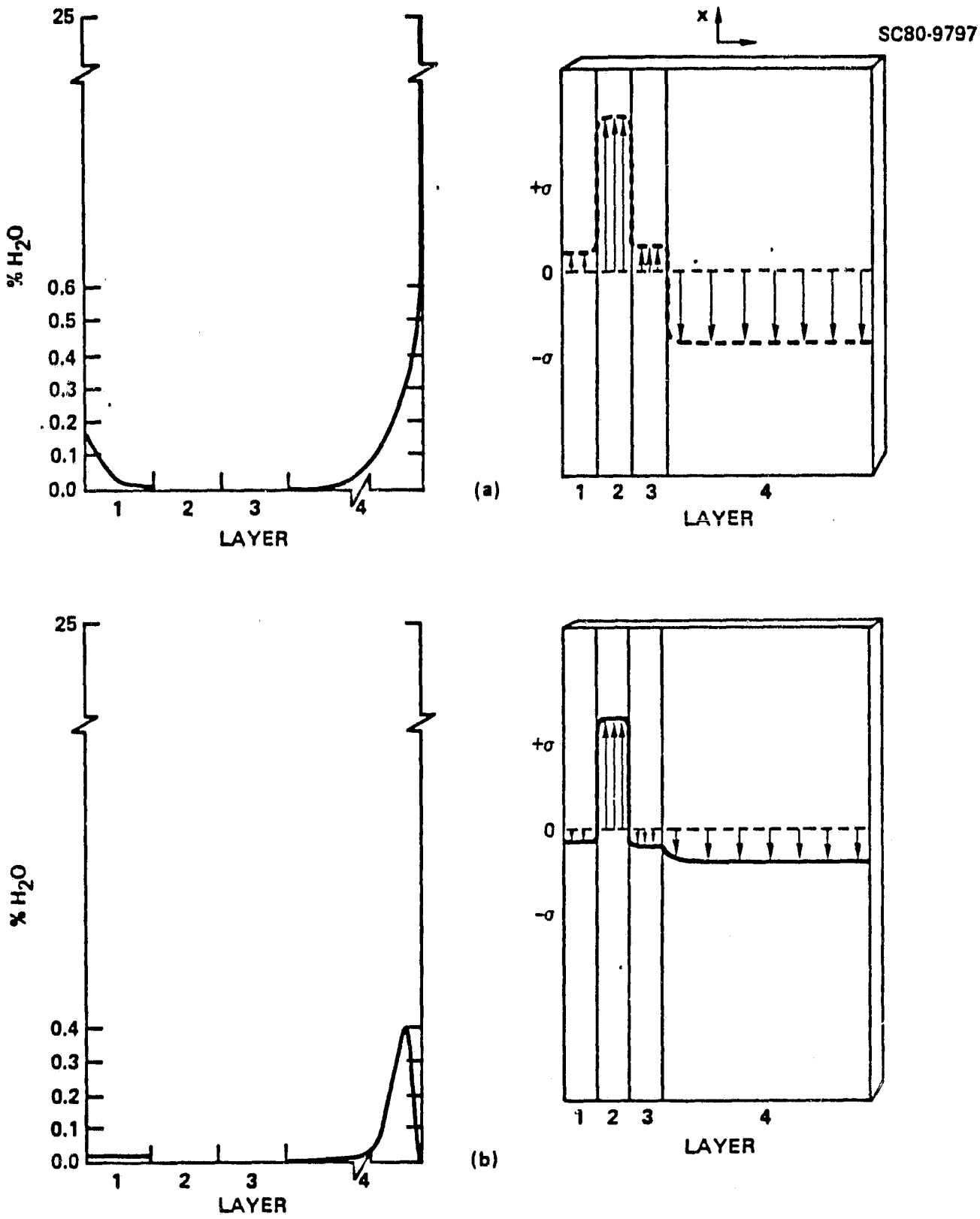

Fig. 20 (a) 1st interval, cycle 1; and (b) 2nd interval, cycle 1.

concentration gradient near the surface in lower Fig. 20. The important cumulative effect of repeating these hydro-thermal exposure cycles is shown in the curves of Fig. 21.

Repetition of the hydrothermal cycles shown in Fig. 19 leads to a cumulative buildup of moisture concentration in the fiber board layer 4. The resultant increased biaxial compressive stress in layer 4 is counter balanced by increasing biaxial tension in the silicon solar cell in layer 2. The life prediction presented by the HTSA model is evaluated by the stress σ in each layer divided by the allowed stress σ(Allowed) which represents the strength reduced by a margin of stress representing the allowed failure probability. The upper curves of Fig. 21 show the safety margin for the silicon wafer diminish as moisture accumulates in the fiber board in the lower curves of this illustration. The four layer solar cell is predicted to fail in about three six day cycles of alternate hydration and drying.

The effect of a fifth layer cell layer of a thin (0.003 in) moisture barrier coating on the predicted moisture build and safety margin curves are shown in the two right curves of Fig. 21. The HTSA inputs which describe these protective coatings are described in Table 4. Addition of this thin layer of EVA or the less permeable Kel-F coating is shown in Fig. 21 to substantially delay but not change the failure mechanism described for the uncoated solar cell. The Kel-F barrier coating was chosen for its extremely low moisture permeability coefficient which is 300 times lower than polyethylene.

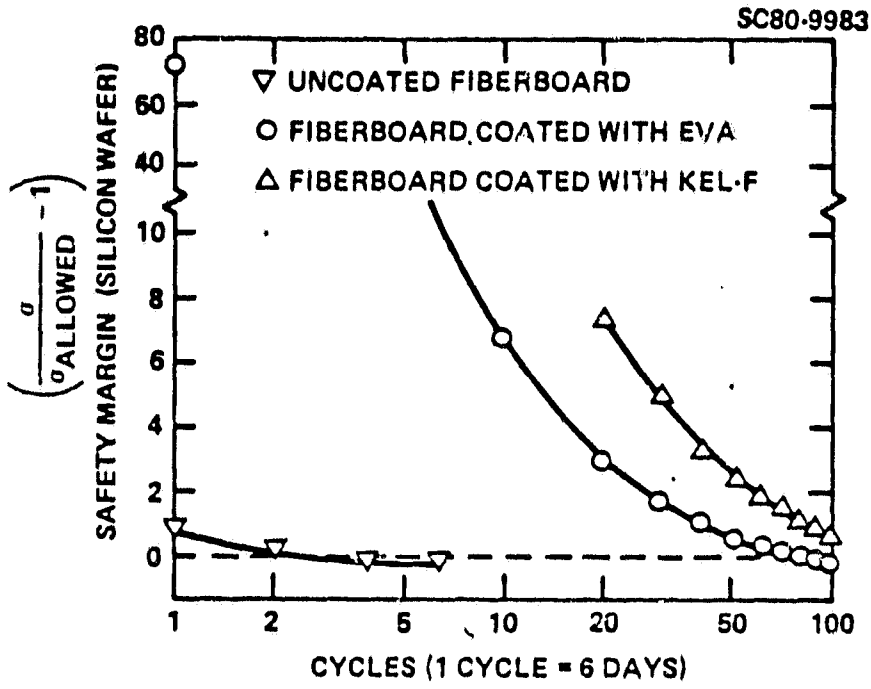

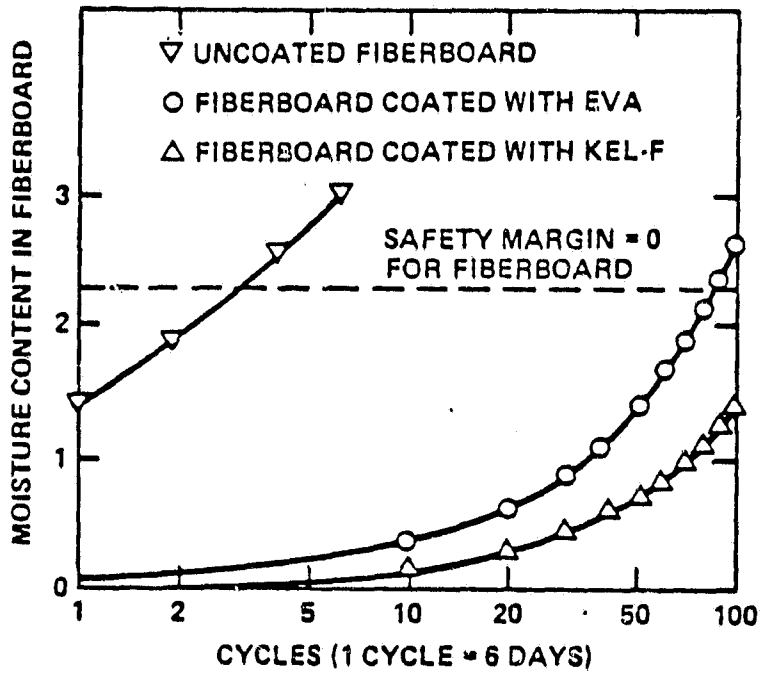

Fig. 21 Moisture content and safety margins of fiberboard in encapsulated solar cell.

Table 4 HTSA Model Imputs for Moisture Barrier Coatings (Layer 5, Fig. 19)

```
            LAYER 5 = CLEAR EVA
            LAYER THICKNESS     H = .0030 INCHES
            THERMAL CONDUCTIVITY = .15000 BTU/(HR-FT-F)
            DENSITY = 57.00000LBM/(FT**3)
            FOR TEMPERATURE LESS THAN      .0 DEGREE C      D = .200E-02EXP(   -3000.0/TEMP.)  MM**2/SEC.
            FOR TEMPERATURE GREATER THAN   .0 DEGREE C      D = .570E 00EXP(   -5000.0/TEMP.)  MM**2/SEC.
            TEMP. IS IN DEGREE K
            BOUNDARY CONCENTRATION IS GIVEN BY EQUATION     C = .001500 *HUM.** 1.00

            MATERIAL 5 IS CLEAR EVA

 E(L) =    20000.    E(T) =   20000.     G(LT) =  600.      ALPHW(L) =  .0000800
U(LT) =  .5000   ALPHA(L) =  .0002000  ALPHA(T) = .0002000  ALPHW(T) =  .0000800
     DEFAULTS        TAU =     0     THICKNESS = .0030

SIGA(L) =  1890.     SIGA(T) =  1890.     SIGA(LT) =  110.
SIGA(L) = -1890.     SIGA(T) = -1890.                          N,M,Q=AXIAL,MOMENT, SHEAR LOAD

            LAYER 5 = KEL-F
            LAYER THICKNESS     H =  .0030 INCHES
            THERMAL CONDUCTIVITY =  .15000 BTU/(HR-FT-F)
            DENSITY =  57.00000LBM/(FT**3)
            FOR TEMPERATURE LESS THAN      .0 DEGREE C      D =  .600E-06EXP(   -30000.0/TEMP.)  MM**2/SEC.
            FOR TEMPERATURE GREATER THAN  .0 DEGREE C       D =  .570E 00EXP(    -5000.0/TEMP.)  MM**2/SEC.
            TEMP. IS IN DEGREE K
            BOUNDARY CONCENTRATION IS GIVEN BY EQUATION     C =  .000400 *HUM.** 1.00

            MATERIAL 5 IS POLYTRIFLUOROCHLOROETHYL

 E(L) =   20000.      E(T) =    20000.     G(LT) =     600      ALPHW(L) =  .0000800
U(LT) =  .5000    ALPHA(L) =  .0002000  ALPHA(T) =  .0002000   ALPHW(T) =  .0000800
     DEFALULTS       TAU =      0    THICKNESS =  .0030

SIGA(L) =  1890.    SIGA(T) =  1890.    SIGA(LT) =  110.
SIGA(L) = -1890.    SIGA(T) = -1890.                          N,M,Q=AXIAL,MOMENT,SHEAR LOAD
```

5.3 Hydro-thermal Cell Cracking and Corrosion

Experimental solar cells of the type studied by E. Laue and A. Gupta at JPL[12] were provided for study at the Science Center. One cell was hydrothermally aged at combined high humidity (100% R.H.) and temperature (75°C) and cell cracking as predicted by the HTSA model calculations occurred in 8 days. The type of cells and the pattern of very open cracks in the cell surface are shown in the photo views of Fig. 22. These hydrothermal cracks opened sufficiently due to fiberboard swelling to break the semi-ductile metallization on the cell front surface. Delamination cracks within the fiber board were also noted by edge examination of the hydrothermally aged cells.

AC impedance measurements readily detect the damage effects of hydrothermal aging and cell cracking as shown in the plots of Z' versus frequency in Fig. 23 and the Cole-Cole plots of Fig. 24. These curves show an approximate five fold reduction in the shunt resistance R_{SH} of the hydrothermally cracked solar cell. These abrupt and major changes in solar cell response are easily recognizable in a solar array as discussed in Appendix II.

In order to understand the role that corrosion plays in a selected failure mechanism of Low Cost Solar Cells, surface analysis has been made using Auger electron spectroscopic profiling. A particular failure mode which was considered was that of cell cracking. Although cracking may or may not be induced by corrosive mechanisms, the resulting void produced by a crack allows a region for possible concentration of electrolytic impurities which aggravate the failure. Indeed, cracking of one cell may not necessarily produce an

Fig. 22 Photovoltaic cells for hydrothermal aging (left view) and magnified view of lower cell (A8925-2) after 8 days aging at 100% R.H., 75°C showing cracked silicon and metallization (right view).

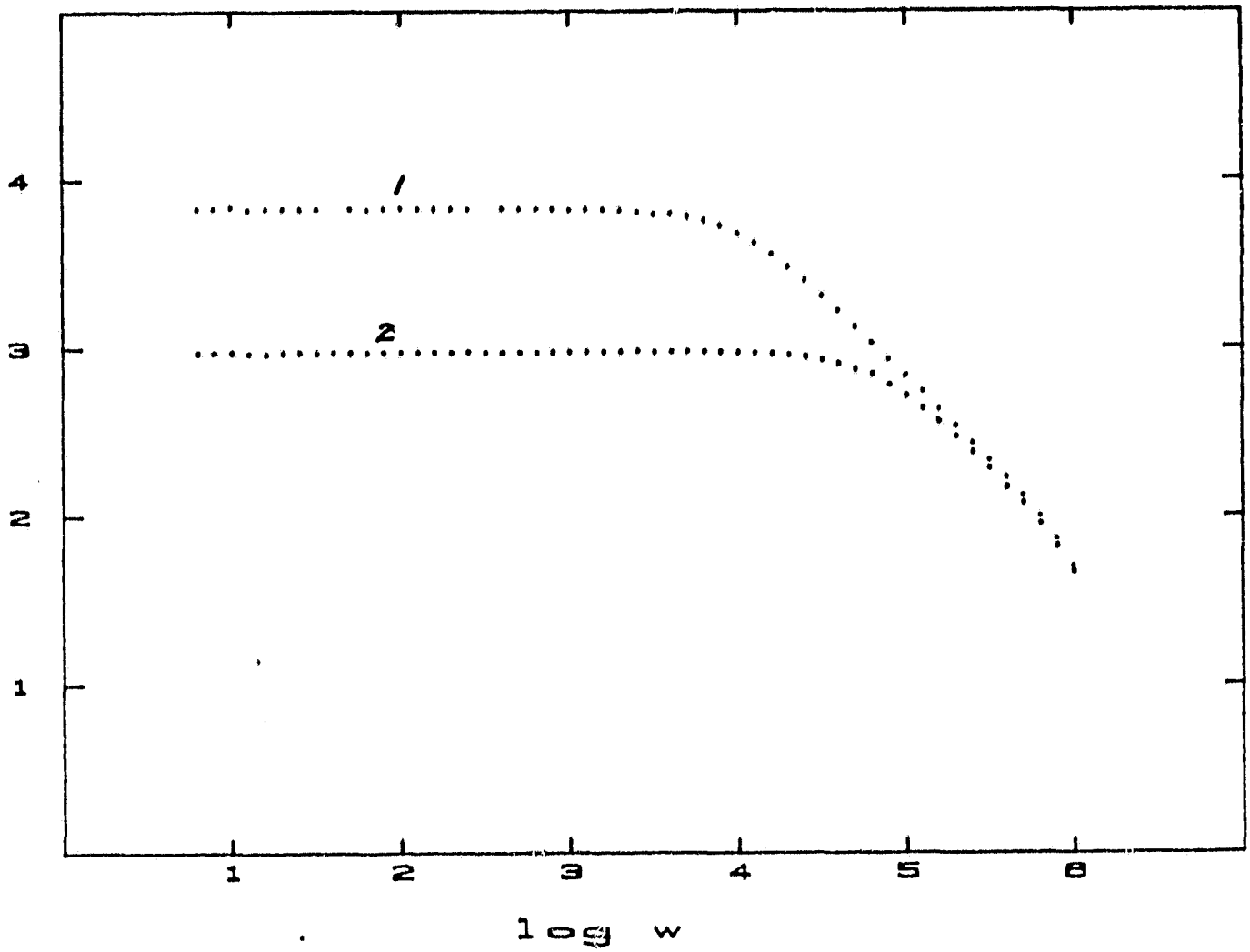

Fig. 23 Log Z vs log ω for EVA encapsulated cell before (#1) and after (#2) exposure to RH 100% at 75°C for 8 days.

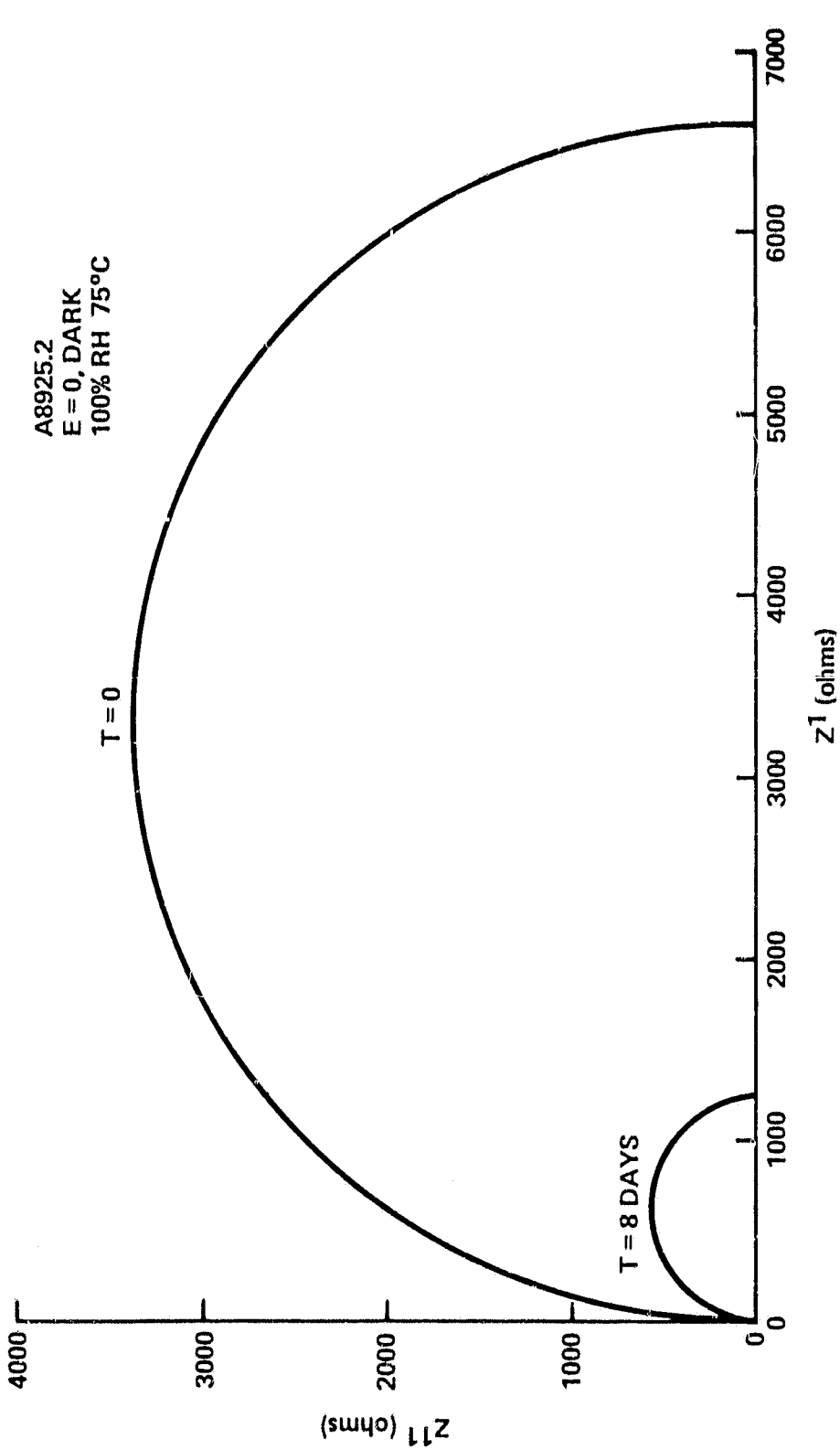

Fig. 24 Cole-Cole plots of AC impedance showing easily identified effects of silicon cell cracking.

immediate failure of an array, but the long term interaction of a corrosive environment could lead to a more serious defect at the crack by forming of current carrying paths which would ultimately short circuit the cell. Work at JPL has shown that corrosion couples to the cracking process.[12]

In order to investigate this possibility, an Auger profile of a fracture surface adjacent to the metallization has been made. The sample was supplied by Dr. Gupta of JPL.[12] The cell was cracked and had been exposed to UV light with intermittent soaks in distilled water. Figure 25 shows a schematic of the fracture surface of the cracked cell. The front surface metallization of the solar cell consisted of a Pb/Sb solder whose major components were Pb, Sn and Fe with observable quantities of S, Cl, K, O, Cr, Ni and C. The substrate (back surface) electrode is a Ni/Pb alloy.

After a 200 sec sputter of superficial organic contamination, the fracture surface of the Si shows primarily Fe, Ni, and Cr distributed as illustrated in the inset in Fig. 25. The fracture surface of the Si also contained significant portions of C and traces of S, Cl, O, and Cu. The distribution suggests a migration of Cr and Fe species from the upper electrode, possibly as a result of a corrosive mechanism. The sample also illustrates some migration of the Ni. The metals which have apparently migrated are expected to be the most active from a thermodynamic point of view since the thermodynamic tendency to electrochemical oxidation takes the following order Cr > Fe > Ni ≈ Pb > Sn. although kinetic aspects of passivation and alloying influences upon chemical potential can produce significant changes in this ordering of actual lability, the selective migration of Fe and

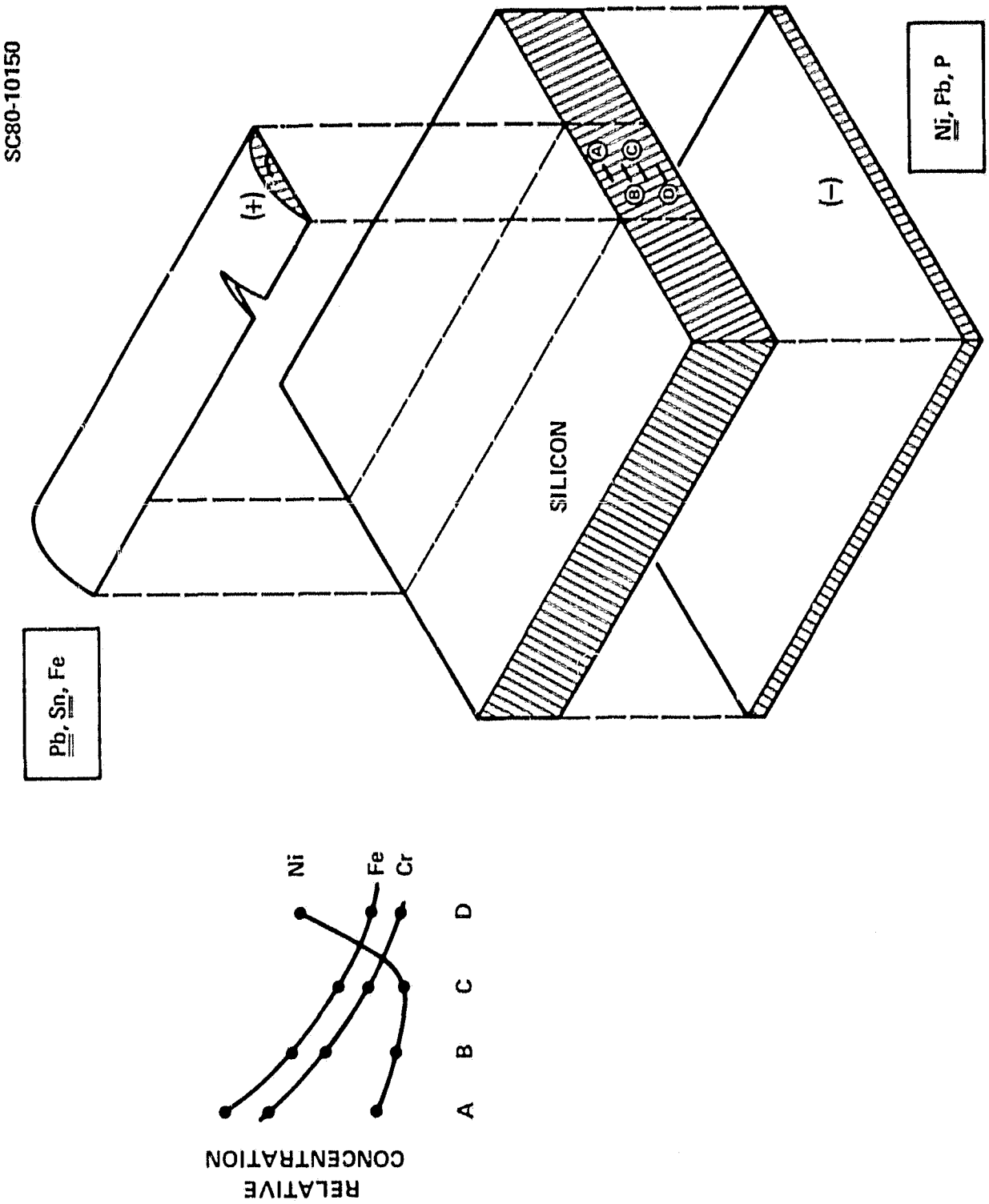

Fig. 25 Schematic of Auger profile of EVA encapsulated solar cell. (underlined elements in high concentration).

Cr from the Pb/Sn electrode which exhibits positive polarity under illumination argues for an electrochemical process leading to the dissolution of Fe nd Cr from the upper electrode.

An additional HTSA computer run was conducted in which moisture exposure was suppressed at 0% R. H. and only the thermal cycle of lower Fig. 19 was imposed on the 4 layer solar cell model. The purely thermoelastic stresses are shown by this computation to be noncritical and noncumulative.

5.4 Interfacial Bonding for Corrosion Protection

A good deal of evidence has been accumulated in the experimental studies of this program that environmentally resistant interface bonding of encapsulant to all solar cell and metallization surfaces is essential for corrosion protection. This problem is even more acute when individual cells display microcracks as discussed in the preceeding sections. The atmospheric corrosion model discussed in earlier sections and summarized in Fig. 11 defines explicit factors for reduction of corrosion rate by suppression of ionic diffusion mechanisms.

In order to extend the theoretical range of this corrosion model, an additional acid-base criteria for interface bond stability, as shown in Fig. 26, will be explored. This criteria was originally developed and verified by Bolger and Michaels[13] and has been incorporated into a general adhesion theory by Kaelble.[14] It is also evident that E. Plueddemann[15]

has recently exploited this system of definition in selection and testing of silane adhesion promoters for LSA. The diagram of Fig. 26 provides a compact graphical method for selecting either acidic (right margin) or basic (left margin) organic radicals to achieve respective high Δ_A or Δ_B with metal oxides (see upper margins) of differing isoelectric points for surfaces (IEPS). Interfaces formed according to the combined criteria Fig. 26 will be tested by atmospheric corrosion monitors and environmental corrosion simulation as already developed in the prior program. Additionally, a new ion migration test method, recently described by Mittal and Lussow[16] will be explored as a small scale screening test for interface stability and corrosion resistance.

SC80-9331

ACIDIC INTERACTIONS

1) **PROBABILITY Δ_A :**

$\Delta_A = IEPS - pK_{A(A)}$

2) **RANGE OF STABILITY:**

$pK_{A(A)} < pH < IEPS$

BASIC INTERACTIONS

1) **PROBABILITY Δ_B**

$\Delta_B = pK_{A(B)} - IEPS$

2) **RANGE OF STABILITY**

$IEPS < pH < pK_{A(B)}$

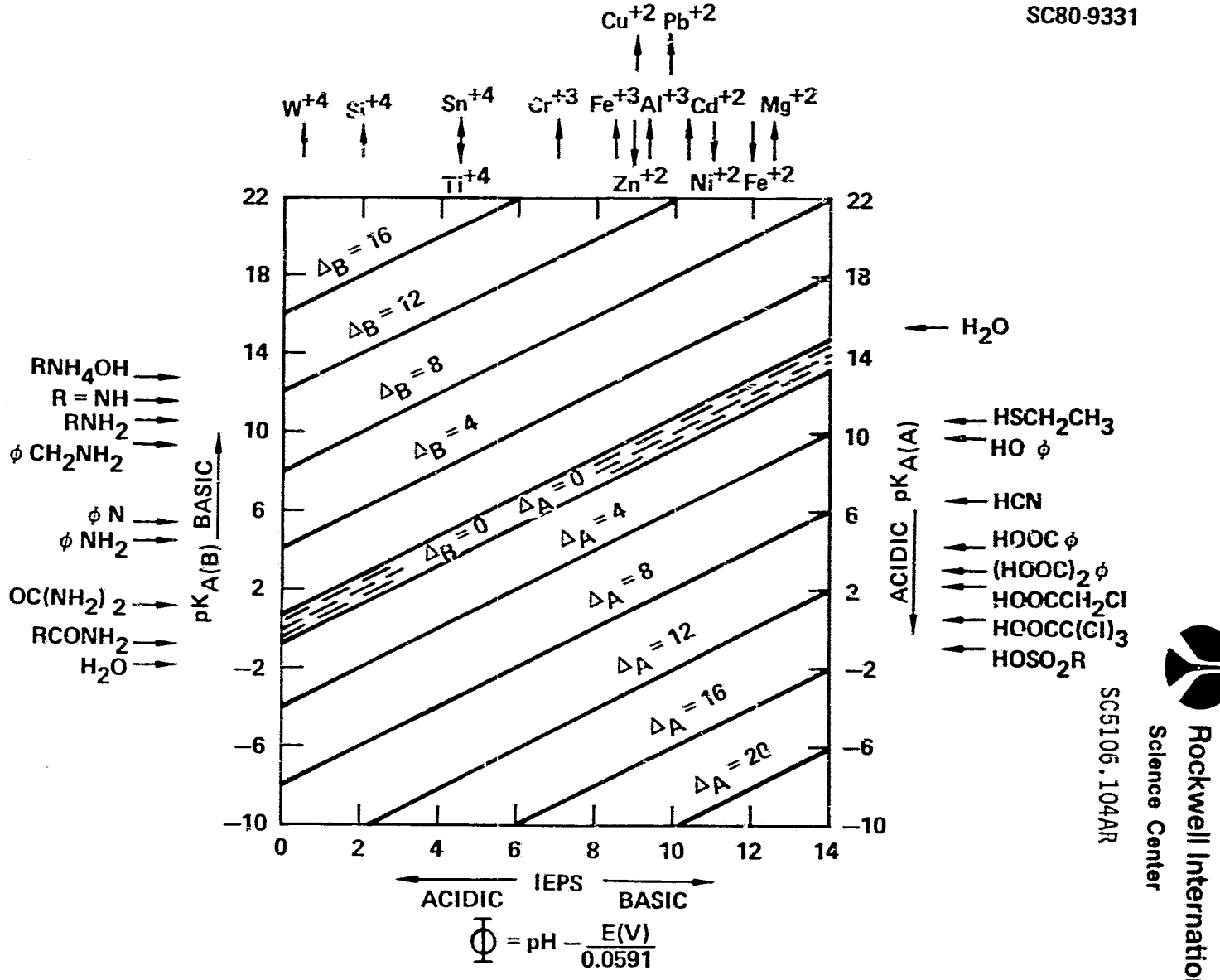

Fig. 26 Acid-base interface stability criteria.

Rockwell International
Science Center

SC5106.104AR

6.0 CONCLUSIONS

Atmospheric corrosion monitors (ACM) have been returned to the Science Center following 13 months deployment at the Mead, Nebraska test site. During this period the ACM units recorded the corrosion protection function of an encapsulant system and correlated Mead climatology with corrosion rates of a nonencapsulated ACM. The fundamental assumptions of a new atmospheric corrosion model were verified in this study. This corrosion model predicts that corrosion rate is the product of a condensation probability (P_c) and the maximum ionic diffusion current (I_L). Encapsulant corrosion protection is specifically related to its efficiency in suppresssing I_L at the potential corrosion interface.

AC impedance measurements combined with impedance spectrum analysis and feed back control to a branch circuit appear as a direct means of remotely locating degraded LSA modules and modifying series to parallel S/P interconnects between modules to achieve maximum LSA power efficiency.

A hydrothermal stress analysis (HTSA) computer model has been successfully applied to evaluate the combined effects of temperature-humidity cycling on development of internal stresses and solar cell cracking in solar cell modules using a fiberboard substrate. The effect of protective polymer coatings of ethylene vinylacetate (EVA) and polytrifluoro-chloroethylene (Kel-F) is to delay but not change the failure process.

A new materials selection criterion for encapsulant bonding is being developed which incorporates both ionic conduction and electrochemical mechanisms of corrosion. The new selection criteria and test methodology are specifically directed at suppressing the micro-corrosion process in the presence of internal defects such as micro-cracks.

7.0 RECOMMENDATIONS

The following specific recommendations in the area of corrosion and encapsulant life prediction are presented from this study:

1. AC impedance monitoring combined with spectrum analysis and feed back control is suggested for field trails at an LSA test site.

2. Develop materials selection criteria and tests for corrosion and environment resistant interfaces with 20-year life capability.

3. Develop and validate a more general reliability and life prediction model for LSA which includes corrosion, interfacial integrity and hydrothermal stress analysis (HTSA) as specialized subjects and directly describes photovoltaic current-voltage (I-V) response.

8.0 NEW TECHNOLOGY

This study has developed and demonstrated new corrosion models and test methods. AC impedance measurements and analysis has been advanced to a potential field deployable state for nondestructive evaluation (NDE) and remote management of LSA branch circuits. Hydrothermal stress analysis (HTSA) has been demonstrated as a method for predicting solar cell life time and failure mechanisms. Atmospheric corrosion monitors (ACM) are effective tools for evaluating atmospheric corrosion resistance of encapsulant bonding materials and evaluating climatology influence on corrosion rates.

9.0 REFERENCES

1. R. G. Ross, Jr., "Photovoltaic Design Optimization for Terrestrial Applications, paper presented at the 13th IEEE Photovoltaic Specialists Conference, Washington, D.C. June 5-8, 1978.
2. R. G. Ross, Jr., "Flat Plate Photovoltaic Design Optimization," presented at the 14th IEEE Photovoltaic Specialists Conference, San Diego, California, Jan. 7-10, 1980.
3. C. Gonzales and R. Weaver, "Cricuit Design Considerations for Photovoltaic modules and Systems," Ibid.
4. R. G. Ross, Jr., C. C. Gonzalez, "Reference Conditions for Reporting Terrestrial Photovoltaic Performance," presented at the AS/ISES 1980 Annual Meeting, Phoenix, Arizona, June 2-6, 1980.
5. D. Schwartz, "Module Performance in a Varying Test Environment," Proceedings of the 11th Project Integration Meeting, JPL Report No. 5101-109 (DOE/JPL-1012-126), October 1978 - December 1978, pp. 3-36 to 3-42.
6. Proceedings of Workshop on "Flat Plate Photovoltaic Module and Array Circuit Design Optimization," Engineering Area, LSA Project, Jet Propulsion Laboratory, March 31 - April 1, 1980.
7. C. L. Leung and D. H. Kaelble, "Moisture Diffusion and Microdamage in Composites," ACS Symposia Series No. 132, American Chemical Society (1980), pp. 419 - 434.

8. N. G. Mc Crum, B. E. Read and G. Williams, "Anelastic and Dielectric Effects in Polymeric Solids," Wiley, New York, (1967), Chap. 4.

9. L. B. Bucciarelli, "Power Loss in Photovoltaic Arrays Due to Mismatch in Cell Characteristics," Solar Energy, 23 (1979), p. 277.

10. F. Manfeld and J. V. Kenkel, "Electrochemical Measurements of Time-of-Wetness and Atmospheric Corrosion Rates," Corrosion, 33(1), (1977), p. 13.

11. D. Kaelble, F. Mansfeld, S. Jeanjaquet and M. Kendig, "Atmospheric Corrosion Model and Monitor for Low Cost Solar Arrays," Proc. Corrosion 81, Toronto, Canada, April 6-10 (1981).

12. E. Laue and A. Gupta, "Reactor for Simulation and Acceleration of Solar Ultraviolet Damage," JPL Report No. 5101-135 (DOE/JPL 1012-31) for Low-Cost Solar Array Project, Sept. 21, 1979.

13. J. C. Bolger and A. S. Michaels, "In Interface Conversion (Editor: P. Weiss) Elsevier, Amsterdam (1968), Chap. I.

14. D. H. Kaelble, Physical Chemistry of Adhesion, Wiley-Intersecion, New York (1971), Chap. 5-5.

15. E. P. Plueddemann, "Chemical Bonding Technology for Terrestrial Solar Cell Modules," JPL Report No. 5101-132 for Low-Cost Solar Array Project, Sept. 1, 1979.

16. K. L. Mittal and R. O. Lussow, "Adhesion Measurement of Polymeric Films and Coatings with Special Reference to Photoresist Materials," in Adhesion and Adsorption of Polymers, (Editor L. H. Lee) Polymer Science and Technology Series Vol. 12B, Plenum Press, New York, 1979, pp. 503-520.

APPENDIX I

MATHEMATICAL RELATIONS FOR CURRENT-VOLTAGE (I-V) RESPONSE IN SINGLE SOLAR CELLS

Introduction

It is often useful to develop an analog model of physical response in order that the interrelations between variables are more fully understood. The model for I-V response presented here is mathematically simple and yet resembles many aspects of real physical response of single solar cells. Of particular interest in this discussion is the analytical description of the fill factor (F), and the maximum power point W_m of the I-V curve which describes cell power generating efficiency. Table 1 summarizes the symbols and nomenclature used in this discussion.

General Relations

Let us assume that short circuit current I_o is proportional to insolation S:

$$I_o = I_D + K_1 S \tag{1}$$

and that the open circuit voltage V_o decreases with increased temperature T and insolation S as follows:

$$V_o = V_D - K_2 (T + K_3 S) \tag{2}$$

where K_1, K_2, and K_3 are positive constants. By introduction of a shape factor K, which is defined as follows:

$$K = \frac{1}{V_o} \ln\left(\frac{R_S + R_{SH}}{R_S}\right) \tag{3}$$

where R_S and R_{SH} are respective series and shunt resistance the IV curve can be expressed as follows:

$$I = I_o \lambda^{-1} [1 - \exp K(V - V_o)] \tag{4}$$

$$\lambda = 1 - \exp(- KV_o) \tag{5}$$

Determining R_S and R_{SH}

By differentiation of Eq. (4) for constant I_o, V_o, and K we obtain the following relation:

$$\frac{dI}{dV} = -KI_o\lambda^{-1} [\exp K(V - V_o)] \tag{6}$$

At the open circuit condition, where $V = V_o$ and $I = 0$, Eq. (6) becomes:

$$\frac{dI}{dV} = -KI_o\lambda^{-1} = \frac{-1}{R_S} \tag{7}$$

At the short circuit condition, where $V = 0$ and $I = I_0$, Eq. (6) becomes

$$\frac{dI}{dV} = -KI_0\lambda^{-1}\,[\exp(-\,KV_0)] = \frac{-1}{R_{SH} + R_S} \tag{8}$$

The limiting slopes of the I-V curve are defined by Eq. (7) to determine R_S at $V = V_0$ and $R_S + R_{SH}$ at $I = I_0$.

Determining the IV Fill Factor F

The fill factor of an IV curve is defined by the following integral relation:

$$F = \frac{1}{I_0 V_0}\int_0^{V_0} I\,dV \tag{9}$$

By substituting Eq. (4) into Eq. (9) we obtain:

$$F = \frac{\lambda^{-1}}{V_0}\int_0^{V_0}[1 - \exp K(V - V_0)]\,dV$$

$$= \frac{\lambda^{-1}}{V_0}\int_0^{V_0} dV - \frac{\lambda}{V_0}\int_0^{V_0}[\exp K(V - V_0)]\,dV \tag{10}$$

Integrating Eq. (10) by parts we obtain the following relation:

$$F = \lambda^{-1} - \frac{\lambda^{-1}}{KV_0}[1 - \exp(-\,KV_0)] \tag{11}$$

Substituting Eq. (5) into Eq. (11) provides the following relation:

$$F \approx \frac{1}{\lambda} - \frac{1}{KV_o} \tag{12}$$

as shown by Eq. (12) when $KV_o \approx 0$ the fill factor $F \approx 0.50$ and when KV_o achieves high values $KV_o > 50$ the fill factor approaches unity.

Determining the Maximum Power Voltage

The power output W of the solar cell is determined by the following product:

$$W = IV \tag{13}$$

The maximum power point, with respect to voltage V, is obtained by differentiating Eq. (13) as follows:

$$\frac{dW}{dV} = I + V\frac{dI}{dV} \tag{14}$$

By solving for maximum power where $dW/dV = 0$ and in substitution of Eq. (4) and Eq. (6) into Eq. (14) we obtain the following expression:

$$\frac{dW}{dV} = \frac{I_o}{\lambda}\left[1 - \exp K(V - V_o)\right] - \frac{VI_o}{\lambda} K \exp K(V - V_o) = 0 \tag{15}$$

By simplification and rearrangement, Eq. (15) defines the voltage V_m where maximum power W_m is produced from the I-V curve by the following relation:

$$\ln (KV_m + 1) + KV_m = KV_o \tag{16}$$

Solutions to Eq. (16) are obtained by introducing values of KV_m in the left side and solving for KV_o. The subsequent determination of ratio of V_m/V_o versus KV_o is obtained by dividing the input KV_m on the left side of Eq. (16) by the output KV_o on the right side of Eq. (16) to obtain the dimensionless ratio V_m/V_o.

Determining the Maximum Power Output

For a given I-V curve the maximum power output W_m is expressed by the relation:

$$W_m = I_m V_m \tag{17}$$

where I_m and V_m are the respective current and voltage at the maximum power point. The relation for I_m is provided by substitution of $V = V_m$ in Eq. (4) to provide the following relation:

$$I_m = I_o \lambda^{-1} [1 - \exp K(V_m - V_o)] \tag{18}$$

By substituting Eq. (18) into Eq. (17) provides the following relation for maximum power:

$$W_m = I_o \lambda^{-1} V_m [1 - \exp K(V_m - V_o)] \tag{19}$$

Alternatively, the maximum power W_m can be reduced by the product $I_o V_o$ to define a maximum power output ratio P_m as follows

$$P_m = \frac{W_m}{I_o V_o} = \frac{V_m \lambda^{-1}}{V_o} [1 - \exp K(V_m - V_o)] \tag{20}$$

Shunt to Series Resistance Ratio

By rearranging Eq. (3) the ratio of shunt to series resistance is given by the following relation:

$$\frac{R_{SH}}{R_S} = \exp (KV_o) - 1 \tag{21}$$

Sample Computations for IV Properties

The procedure for conducting abbreviated calculations for IV response proceeds as shown in Table 2. The calculation proceeds from left to right across each line of Table 2 and from top to bottom through the list of equations in lower Table 2. For convenience, this calculation simply inputs an assigned value of KV_m into Eq. (16) and computes a value of KV_o in the two left columns of Table 2. The dimensionless ratio V_m/V_o is defined and the reciprocal value λ^{-1} calculated as shown in the third and fourth columns of Table 2. The remaining properties F, P_m, and R_{SH}/R_S in the right column of Table 2 are readily calculated to complete the calculations.

It is evident that in full calculations both Eq. (1) and Eq. (2) would be utilized with input of two environment conditions T and S and six

solar cell constants I_D, V_D, K, K_1, K_2, K_3 with computation of I_o and V_o. The next computation inputs given value of KV_o into Eq. (16) and successive values of KV_m substituted to satisfy the equality with a determined value of KV_m as output. Successive steps of the full calculation follow those of the abbreviated procedure of Table 2.

Table 1
List of Principal Current-Voltage (I-V) Design and Performance Parameters

Symbol	Meaning
	Design Parameters
K_1	Coefficient of light developed current
K_2	Thermal coefficient of voltage
K_3	Thermal coefficient of light
I_D	Dark current
V_D	Dark voltage
R_S	Series resistance
R_{SH}	Shunt resistance
	Environment Parameters
T	Ambient temperature
S	Ambient insolation
	Performance Variables
I_o	Short circuit current
V_o	Open circuit voltage
K, λ	Current-voltage (I-V) response factors
F	I-V fill factor
V_m	Voltage at the maximum power point
W_m	Wattage at the maximum power point
I_m	Current at the maximum power point
P_m	Proportion of ideal power output

Table 2
Sample Computations of Solar Cell IV Response

KV_m	KV_o	V_m/V_o	λ^{-1}	F	P_m	R_{SH}/R_S
.001	1.9995E-3	.5001	5.006E2	.50017	.2501	.002
.002	3.9978E-3	.5003	2.506E2	.4991	.2503	.004
.005	9.9875E-3	.5006	1.006E2	.5007	.2506	.0100
.01	1.995E-2	.5012	5.0627E1	.5016	.2512	.0201
.02	3.903E-2	.5025	2.6125E1	.5033	.2525	.0406
.05	9.789E-2	.5061	1.0724E1	.5082	.2562	.1038
.10	1.953E-1	.5120	5.6366	.5162	.2623	.2157
.20	3.823E-1	.5231	3.1474	.5318	.2744	.4657
.50	9.055E-1	.5522	1.6789	.5744	.3090	1.473
1.00	1.693	.5906	1.2254	.6347	.3618	4.436
2.00	3.099	.6455	1.0472	.7245	.4506	2.117E1
5.00	6.792	.7362	1.0011	.8539	.6142	8.895E2
10	1.2398E1	.8066	1.0000	.9193	.7333	2.423E5
20	2.3045E1	.8679	1.0000	.9566	.8266	1.019E10
50	5.3932E1	.9271	1.0000	.9815	.9089	2.6442E23
100	1.0462E2	.9559	1.0000	.9904	.9465	2.728E45
200	2.0530E2	.9742	1.0000	.9951	.9693	∞
500	5.0622E2	.9877	1.0000	.9980	.9857	∞
1000	1.00691E3	.9932	1.0000	.999	.9932	∞

$KV_o = \ell n\ (KV_m + 1) + KV_m$ — IV Shape Factor (Eq. 16)

$V_m/V_o = KV_m/KV_o$ — Max. Power Voltage Ratio

$\lambda^{-1} = 1/[1 - \exp(-KV_o)]$ — Function of Shape Factor (Eq. 5)

$F = \lambda^{-1} - (KV_o)^{-1}$ — IV Fill Factor (Eq. 12)

$P_m = (V_m/V_o)\lambda^{-1}\ [1 - \exp K(V_m - V_o 1)]$ — Max. Power Ratio (Eq. 20)

$R_{SH}/R_S = \exp\ (KV_o) - 1$ — Shunt/Series Resistance (Eq. 21)

APPENDIX II

Analysis for Frequency Dependence of AC Impedance

Introduction

AC (alternating current) impedance measurements have been applied experimentally to LSA (low cost solar array) single solar cells or to modules of 50 to 75 cells electrically connected in series. The AC impedance measurement is conducted by scanning the frequency spectrum from 1 Hz through 1 MHz using low amplitude AC voltage (±10 mV) and constant temperature. The frequency response for AC impedance of a single solar cell appears to fit the classical Debye type[1] single relaxation mechanism. When multiple solar cells are examined, the frequency response for AC impedance is more complex but appears to be well described by a symmetrically broadened frequency distribution of Debye type relaxation processes. The empirical distribution function developed by Cole and Cole provides a set of general equations for broadened AC impedance response which reduce to the Debye single relaxation as a special case. In this discussion, the analysis centers on the Cole-Cole distribution function as a means for evaluating performance parameters of both single solar cells and multiple cells in modules or branch circuits. The AC impedance measurement represents a readily conducted nondestructive test which when combined with the dielectric analysis discussed here becomes a method for conducting nondestructive evaluation (NDE) of LSA performance. A list of the principal parameters of this analysis is presented in Table I.

The Cole-Cole Distribution Function

The characteristic relaxation time τ_0 for the three element circuit shown in Fig. 5 is defined by the following relation:

$$\tau_0 = C\, R_{SH} \tag{1}$$

The storage or in-phase impedance z' is defined as a function of test frequency ω (radians/s) by the following relation:

$$z' = R_S + \frac{R_{SH}\,[1 + (\omega\tau)^{\beta}\cos(\beta\pi/2)]}{1 + (\omega\tau)^{2\beta} + 2(\omega\tau)^{\beta}\,(\cos\,\beta\pi/2)} \tag{2}$$

The loss or out-of-phase impedance z" is defined as a function of test frequency by the following relation:

$$z'' = \frac{R_{SH}\,(\omega\tau)^{\beta}\sin(\beta\pi/2)}{1 + (\omega\tau)^{2\beta} + 2(\omega\tau)^{\beta}\cos(\beta\pi/2)} \tag{3}$$

The distribution quality factor β is unity, $\beta = 1.0$, for the Debye single relaxation and defines a range $0<\beta<1.0$ for symmetrically broadened distribution with multiple relaxation times.

The Cole-Cole distribution function $\phi(\ln\,\tau)$, is defined by the following relation:

$$\phi(\ln \tau) = \frac{(1/2\pi)\ \sin \beta\pi}{\cosh[\beta \ln (\frac{\tau}{\tau_o})] + \cos \beta\pi} \tag{4}$$

The distribution function Eq. (4) fulfills the following general normalizing relation:

$$\int_{-\infty}^{\infty} \delta(\ln \tau)\ d \ln \tau = 1 \tag{5}$$

The detailed form of the distribution function of Eq. (4) relates to the distribution quality factor β as will be explored in subsequent discussion.

Combining Eq. (2) and Eq. (3) to eliminate $\omega\tau$ provides the following equation for a circle:

$$\left[z' - \left(\frac{R_S + R_{SH}}{2}\right)\right]^2 + \left[z'' + \frac{R_{SH}\ \text{cotan}\ (\beta\pi/2)}{2}\right]^2 = \left[\frac{R_{SH}\ \text{cosec}\ \beta\pi/2}{2}\right]^2 \tag{6}$$

The radius r_c of this circle is:

$$r_c = \frac{R_{SH}}{2}\ \text{cosec}\ (\frac{\beta\pi}{2}) \tag{7}$$

and its ce ter has coordinates:

$$z'_c = \frac{R_{SH} + R_S}{2} \tag{8}$$

$$z'_c = -\frac{R_{SH}}{2}\ \text{cotan}\ (\frac{\beta\pi}{2}) \tag{9}$$

AC impedance data that conform to the Cole-Cole distribution function can be conventionally plotted as a circular function on z' and z" coordinates.

Distribution Analysis of AC Impedance Data

A numerical analysis of AC impedance has been developed by Messrs. Gene Meyer and Gary Lindberg of the Science Center for a least squares circle fit of the Cole-Cole distribution. A schematic representation of the circular least squares fit is illustrated in Fig. 9 where r_c, z'_c, and z''_c are respectively defined by Eqs. (7-9).

The computation is addressed to reducing the distance d_i between the best fit circle and the experimental points represented by z'_i, z''_i. From Fig. 9 we have:

$$d_i = (x_i^2 + y_i^2)^{1/2} \tag{10}$$

$$x_i = z'_i - z'_c - r_c \cos \theta_i \tag{11}$$

$$y_i = z''_i - z''_c - r_c \sin \theta_i \tag{12}$$

where x_i and y_i are the respective z' and z" axis errors between the curve and the point z'_i, z''_i. To obtain the best fit circle to a set of AC impedance data points the objective is to minimize D which is defined from Eq. (1-3) as follows:

$$D = \sum_{i=1}^{n} d_i^2$$

$$= \sum_{i=1}^{n} (z_i' - z_c' - r_c \cos\theta_i)^2 +$$

$$\sum_{i=1}^{n} (z_i'' - z_c' - r_c \sin\theta_i)^2 \qquad (13)$$

By taking the partial deviatives of D in Eq. (13) with respect to x_c', x''_c and r_c and setting $\partial D/\partial x_c' = 0$, $\partial D/\partial x_c''$, and $\partial D/\partial r_c$ equal to zero the following relations are obtained:

$$f = \frac{\partial D}{\partial x_c'} = nx_c' + r_c \sum_{i=1}^{n} \cos\theta_i - \sum_{i=1}^{n} z_i' = 0 \qquad (14)$$

$$q = \frac{\partial D}{\partial x_c''} = nx_c'' + r_c \sum_{i=1}^{n} \sin\theta_i - \sum_{i=1}^{n} z_i'' = 0 \qquad (15)$$

$$h = \frac{\partial D}{\partial r_c} = nr_c + z_c' \sum_{i=1}^{n} \cos\theta_i + z_c'' \sum_{i=1}^{n} \sin\theta_i -$$

$$\sum_{i=1}^{n} z_i' \cos\theta_i - \sum_{i=1}^{n} z_i'' \sin\theta_i = 0 \qquad (16)$$

Inspection of Fig. 9 periods the following relations for sin θ_i in Eqs. (13-16).

$$\sin \theta_i = \frac{z'_i - z'_c}{[(z'_i - z'_c)^2 + (z''_i - z''_c)^2]^{1/2}} \tag{17}$$

$$\cos \theta_i = \frac{z''_i - z''_c}{[z'_i - z'_c)^2 + (z''_i - z''_c)^2]^{1/2}} \tag{18}$$

Inspection of Eqs. (14-16) shows that:

$$\frac{\partial f}{\partial x'_c} = n; \quad \frac{\partial f}{\partial x''_c} = 0; \quad \frac{\partial f}{\partial r_c} = \sum_{i=1}^{n} \cos \theta_i$$

$$\frac{\partial g}{\partial x'_c} = 0; \quad \frac{\partial g}{\partial x''_c} = n; \quad \frac{\partial g}{\partial r_c} = \sum_{i=1}^{n} \sin \theta_i$$

$$\frac{\partial h}{\partial x'_c} = \sum_{i=1}^{n} \cos \theta_i; \quad \frac{\partial h}{\partial x''_c} = \sum_{i=1}^{n} \sin \theta_i; \quad \frac{\partial h}{\partial r_c} = n$$

A set of three equations and the unknowns is expressed by Eqs. (14-16). Solution of these equations can be accomplished by use of a three parameter analog of the Newton-Raphson method as described by Henrici.[2] Expanding the example of two equations and two unknowns described by Henrici to our case, provides the following determinant relations, where K and K + 1 represent successive iterations where $x'_c = (x'_c)_K$, $x''_c = (x'_c)_K$ and $r_c = (r_c)_K$:

$$M_K = \left| \begin{array}{ccc} \frac{\partial f}{\partial x'_c} & \frac{\partial f}{\partial x''_c} & \frac{\partial f}{\partial r_c} \\ \frac{\partial g}{\partial x'_c} & \frac{\partial g}{\partial x''_c} & \frac{\partial g}{\partial r_c} \\ \frac{\partial h}{\partial x'_c} & \frac{\partial h}{\partial x''_c} & \frac{\partial h}{\partial r_c} \end{array} \right|_K \tag{19}$$

$$(z'_c)_{K+1} = (z'_c)_K + \frac{\left| \begin{array}{ccc} -f & \frac{\partial f}{\partial x''_c} & \frac{\partial f}{\partial r_c} \\ -g & \frac{\partial g}{\partial x''_c} & \frac{\partial f}{\partial r_c} \\ -h & \frac{\partial h}{\partial x''_c} & \frac{\partial h}{\partial r_c} \end{array} \right|_K}{M_K} \tag{20}$$

$$(z''_c)_{K+1} = (z''_c)_K + \frac{\left| \begin{array}{ccc} \frac{\partial f}{\partial x'_c} & -f & \frac{\partial f}{\partial r_c} \\ \frac{\partial g}{\partial x'_c} & -g & \frac{\partial g}{\partial r_c} \\ \frac{\partial h}{\partial x'_c} & -h & \frac{\partial h}{\partial r_c} \end{array} \right|_K}{M_K} \tag{21}$$

$$(r_c)_{K+1} = (r_c)_K + \frac{\begin{vmatrix} \frac{\partial f}{\partial x'_c} & \frac{\partial f}{\partial x''_c} & -f \\ \frac{\partial g}{\partial x'_c} & \frac{\partial g}{\partial x''_c} & -g \\ \frac{\partial h}{\partial x'_c} & \frac{\partial h}{\partial x''_c} & -h \end{vmatrix}_K}{M_K} \tag{22}$$

The computation initiates at K = 1 by selection of three widely separated experimental points (z'_i, z''_i) in the graph of Fig. 9 in order to make a good initial estimate of x'_c, x''_c and r_c for K = 1 by triangulation.

Using these values of x'_c, x''_c, and r_c one sums over the data set to obtain the following summations:

$$\sum_{i=1}^{n} z'_i; \quad \sum_{i=1}^{n} z''_i$$

which remain constant through subsequent iterations. Additionally summations are made for each iteration K for the following:

$$\sum_{i=1}^{n} \sin\theta_i; \quad \sum_{i=1}^{n} \cos\theta_i; \quad \sum_{i=1}^{n} z'_i \cos\theta_i; \quad \sum_{i=1}^{n} z''_i \sin\theta_i$$

which will correlate with the introduced values of $(z'_c)_K$, $(z''_c)_K$, $(r_c)_K$ into Eqs. (17-18). The above summations are introduced into Eq. (14-16) to solve for the K iteration values of f, g, and h and M_K from Eq. (19).

The above K iteration coefficients are applied in Eqs. (19-22) to obtain the K + 1 iteration solutions for x'_c, x''_c and r_c. These iterative calculations continue until terminated by an appropriate convergence test condition, such as:[3]

$$0 < \left| \frac{(Q_{K+1} - Q_K)^2}{Q_K - Q_{M-1}} \right| < \varepsilon_{K+1} \tag{23}$$

where Q represents the respective coefficients z'_c or z''_c or r_c for the K+1, K, and K-1 iterations and ε_{K+1} the assigned convergence condition for obtaining a final solution where:

$$Q = Q_{K+1} \pm \varepsilon_{K+1} \tag{24}$$

and Q is the best value of the respective coefficients z'_c, z''_c and r_c. The iteration calculation is completed by satisfying Eq. (23). The radial standard deviation δ_r of experimental points to the calculated radius r_c is obtained by utilizing the parameter D from Eq. (13) in the following conventional relation

$$\delta_r = \left(\frac{D}{n-1}\right)^{1/2} \tag{25}$$

Summary

The above definitions and computational procedures provide a means of isolating significant solar cell performance parameters. For example, by mea-

suring a limited frequency range of AC impedance response this analysis permits direct calculation of the shunt R_{SH} and series R_S resistances of the LSA module or branch circuit. By direct measurement R_S and R_{SH} are evaluated as the respective high and low frequency asymptotes of a broad range of frequency measurements. This analysis also provides a direct method for evaluating the uniformity of single cell responses within the solar array in terms of the Cole-Cole distribution function. This analysis is currently incorporated in a micro-computer program for AC impedance evaluation of LSA.

References

1. N. G. McCrum, B. E. Read, and G. Williams, Anelastic and Dielectric Effects in Polymeric Systems, Wiley, New York (1967), pp. 102-140.
2. P. Henrici, Elements of Numeric Analysis, Wiley, New York (1964), pp 105-107.
3. A. Ralston, "A First Course in Numerical Analysis," McGraw Hill, New York (1955), pp. 328-332.

Table 1

List of Principal AC Impedance Measurements
and Performance Parameters

Symbol	Meaning
	Measurement Parameters
z'	Storage component of AC impedance at frequency ω
z''	Loss component of AC impedance at frequency ω
$\omega = 2\pi f$	Test frequency (rad/s)
	Impedance Response
R_{SH}	Shunt resistance
R_S	Series resistance
C	Capacitance
β	Cole-Cole shape factor ($0<\beta<1.0$)
τ_0	Characteristic relaxation time
	Parameters of Cole-Cole Numeric Analysis
r_c	Mean radius of Cole-Cole arc
z'_c	Center of storage axis of Cole-Cole arc
z''_c	Center of loss axis of Cole-Cole arc
δ_r	Standard deviation of the mean radius r_c